AGU PUBLICATIONS

JGR

Journal of Geophysical Research: Atmospheres

RESEARCH ARTICLE
10.1002/2014JD022963

**Key Points:**
- New method of analyzing primary marine aerosol (PMA) number size distributions
- PMA <15% of aerosol number concentrations, <58% of CCN in E–PEACE
- CDNC increased with increasing >100 nm particles in E-PEACE but not SOLEDAD

**Supporting Information:**
- Texts S1–S6 and Figures S1–S7

**Correspondence to:**
L. M. Russell,
lmrussell@ucsd.edu

**Citation:**
Modini, R. L., et al. (2015), Primary marine aerosol-cloud interactions off the coast of California, *J. Geophys. Res. Atmos.*, *120*, 4282–4303, doi:10.1002/2014JD022963.

Received 8 DEC 2014
Accepted 13 APR 2015
Accepted article online 16 APR 2015
Published online 14 MAY 2015



# Primary marine aerosol-cloud interactions off the coast of California

**R. L. Modini[1,2], A. A. Frossard[1,3], L. Ahlm[1,4], L. M. Russell[1], C. E. Corrigan[1], G. C. Roberts[1,5], L. N. Hawkins[6], J. C. Schroder[7,8], A. K. Bertram[7], R. Zhao[9], A. K. Y. Lee[9], J. P. D. Abbatt[9], J. Lin[10], A. Nenes[11], Z. Wang[12], A. Wonaschütz[13], A. Sorooshian[12], K. J. Noone[14], H. Jonsson[15], J. H. Seinfeld[16], D. Toom-Sauntry[17], A. M. Macdonald[17], and W. R. Leaitch[17]**

[1]Scripps Institution of Oceanography, University of California, San Diego, La Jolla, California, USA, [2]Now at École Polytechnique Fédérale de Lausanne, Lausanne, Switzerland, [3]Now at Department of Chemistry, University of California, Berkeley, California, USA, [4]Now at Department of Applied Environmental Science (ITM) and the Bolin Centre for Climate Research, Stockholm University, Stockholm, Sweden, [5]Centre National de la Recherche Scientifique-Groupe d'études de l'Atmosphère Météorologique, Toulouse, France, [6]Department of Chemistry, Harvey Mudd College, Claremont, California, USA, [7]Department of Chemistry, University of British Columbia, Vancouver, British Columbia, Canada, [8]Now at Department of Chemistry and Biochemistry and CIRES, University of Colorado Boulder, Boulder, Colorado, USA, [9]Department of Chemistry, University of Toronto, Toronto, Ontario, Canada, [10]School of Earth and Atmospheric Sciences, Georgia Institute of Technology, Atlanta, Georgia, USA, [11]School of Earth and Atmospheric Sciences, and School of Chemical and Biomolecular Engineering, Georgia Institute of Technology, Atlanta, Georgia, USA, [12]Department of Chemical and Environmental Engineering, and Department of Atmospheric Sciences, University of Arizona, Tucson, Arizona, USA, [13]Faculty of Physics, University of Vienna, Vienna, Austria, [14]Department of Applied Environmental Science, Stockholm University, Stockholm, Sweden, [15]Center for Interdisciplinary Remotely-Piloted Aerosol Studies, Marina, California, USA, [16]Department of Chemical Engineering, California Institute of Technology, Pasadena, California, USA, [17]Science and Technology Branch, Environment Canada, Toronto, Ontario, Canada

**Abstract** Primary marine aerosol (PMA)-cloud interactions off the coast of California were investigated using observations of marine aerosol, cloud condensation nuclei (CCN), and stratocumulus clouds during the Eastern Pacific Emitted Aerosol Cloud Experiment (E-PEACE) and the Stratocumulus Observations of Los-Angeles Emissions Derived Aerosol-Droplets (SOLEDAD) studies. Based on recently reported measurements of PMA size distributions, a constrained lognormal-mode-fitting procedure was devised to isolate PMA number size distributions from total aerosol size distributions and applied to E-PEACE measurements. During the 12 day E-PEACE cruise on the R/V *Point Sur*, PMA typically contributed less than 15% of total particle concentrations. PMA number concentrations averaged 12 $cm^{-3}$ during a relatively calmer period (average wind speed 12 $m/s^{1}$) lasting 8 days, and 71 $cm^{-3}$ during a period of higher wind speeds (average 16 $m/s^{1}$) lasting 5 days. On average, PMA contributed less than 10% of total CCN at supersaturations up to 0.9% during the calmer period; however, during the higher wind speed period, PMA comprised 5–63% of CCN (average 16–28%) at supersaturations less than 0.3%. Sea salt was measured directly in the dried residuals of cloud droplets during the SOLEDAD study. The mass fractions of sea salt in the residuals averaged 12 to 24% during three cloud events. Comparing the marine stratocumulus clouds sampled in the two campaigns, measured peak supersaturations were 0.2 ± 0.04% during E-PEACE and 0.05–0.1% during SOLEDAD. The available measurements show that cloud droplet number concentrations increased with >100 nm particles in E-PEACE but decreased in the three SOLEDAD cloud events.

## 1. Introduction

Primary marine aerosol (PMA) is a globally important natural source of atmospheric aerosol particles. PMA consists of sea salt and ocean-derived organic species and is also known as "sea spray aerosol" or SSA [*de Leeuw et al.*, 2011]. PMAs play crucial roles in a range of atmospheric chemistry processes [*Finlayson-Pitts and Hemminger*, 2000; *Osthoff et al.*, 2008], and the direct [*Murphy et al.*, 1998; *Quinn and Coffman*, 1999; *Randles et al.*, 2004] and indirect (cloud) effects [*Woodcock*, 1952; *Pierce and Adams*, 2006] of aerosols on climate. Quantification of these effects generally requires knowledge of the number size distribution of PMA particles in the ambient atmosphere.

For example, to evaluate PMA-cloud interactions and PMA indirect climate effects, it is necessary to know the number and size of PMA particles that act as cloud condensation nuclei (CCN) in a given supersaturated environment. These questions cannot be answered from knowledge of PMA mass concentrations alone

[*Andreae and Rosenfeld*, 2008]. Marine aerosols are always composed of a number of different particle types (e.g., nonsea-salt (nss) sulfates and continental aerosols) [*Shank et al*., 2012; *Clarke et al*., 2013; *Frossard et al*., 2014]; and it is difficult to separate the number of PMA-containing particles based on measured mass concentrations. Consequently, ambient PMA number concentration data are scarce, and the contribution of PMA to CCN populations and the aerosol indirect effect is poorly constrained.

*Lewis and Schwartz* [2004] reviewed ambient PMA number-based measurements prior to 2004. Observed bulk concentrations vary greatly from well below 1 $cm^{-3}$ to greater than 200 $cm^{-3}$, with most values falling below 50 $cm^{-3}$. These numbers contrast with total particle concentrations of 200–800 $cm^{-3}$ typically observed in the clean Marine Boundary Layer (MBL) [*Fitzgerald*, 1991; *Heintzenberg et al*., 2000], which suggests that PMA only rarely contributes more than 25% of total marine aerosol number concentrations.

Some dependence of PMA number concentration on local wind speed is usually observed, consistent with the fact that sea spray particles are generated from processes associated with the agitation of the sea surface by air moving above it (mainly breaking wave-bubble cloud-whitecap formation). However, the relationship between PMA concentration and wind speed is complex [*Grythe et al*., 2014]. It is complicated by uncertainties in PMA number concentration measurements and the fact that in the marine boundary layer, PMA particles from different sources accumulate over days and locations.

The PMA number size distribution peaks below 1 μm dry particle diameter ($D_p$; for sea-salt particles whose growth factor at 80% relative humidity (RH) is approximately 2, $D_p$ is approximately equal to particle radius at 80% RH, $r_{80}$, which is another commonly used metric of PMA particle size) [*de Leeuw et al*., 2011]. However, measurements of the precise position and shape of the peak vary considerably. The ambient PMA size distributions generally peak in the $r_{80}$ range 0.2–0.5 μm, which reflects the fact that the size mode of PMA is larger than Aitken (~0.02–0.08 μm) and accumulation (~0.08–0.2 μm) mode particles [*Lewis and Schwartz*, 2004]. *Lewis and Schwartz* [2004] defined a canonical PMA size distribution that captured the majority of measurements they reported to within a factor of 3. The canonical distribution consists of a single, broad lognormal mode (mean = 0.3 μm, geometric standard deviation = 2.8) whose amplitude scales with the square of the wind speed (10 m above the ocean surface, $U_{10}$). The distribution was restricted to the range 0.1–25 μm $r_{80}$ since there were few measurements showing the existence of significant numbers of PMA particles in the atmosphere with $r_{80}$ below 0.1 μm.

More recently, there has been considerable evidence that sub-0.1 μm $D_p$ PMA particles are in fact emitted directly into the atmosphere [*de Leeuw et al*., 2011; *Quinn and Bates*, 2011]. The new evidence chiefly consists of laboratory-based bubble bursting studies, in which PMA size distributions were produced in continuous bubbling chambers that peaked in the $D_p$ range 0.05–0.1 μm [*Sellegri et al*., 2006; *Keene et al*., 2007; *Fuentes et al*., 2010; *Modini et al*., 2010; *Bates et al*., 2012; *Zábori et al*., 2012]. Verification has been provided by volatility [*Clarke et al*., 2006; *Blot et al*., 2013], combined volatility and hygroscopicity [*Cravigan et al*., 2015], electron microscopy, and mass spectrometry [*Murphy et al*., 1998; *Lawler et al*., 2014] field observations of sub-0.1 μm $D_p$ PMA particles.

A recent study conducted in a sealed wave channel in the Hydraulics Laboratory of Scripps Institution of Oceanography directly measured the size distribution of PMA generated from whitecaps produced by actual breaking waves [*Prather et al*., 2013], which may be more representative of PMA production in the open ocean than simpler bubbling setups. This distribution is well represented by a single lognormal mode that peaks at larger $D_p$ (mean = 0.16 μm) and is broader (geometric standard deviation = 3) than the size distributions measured in the continuous bubbling chamber studies cited above. The breaking wave size distribution measured in the Scripps wave channel was remarkably constant over a range of water conditions [*Collins et al*., 2013]. This study, along with the canonical PMA size distribution defined by *Lewis and Schwartz* [2004], suggests that the PMA size distribution can be fairly well represented by a single, broad lognormal mode centered at 0.16–0.3 μm $D_p$. This representation encompasses ultrafine ($D_p < 0.1$ μm) and large submicrometer ($D_p > 0.3$ μm) PMA particles of different chemical compositions (e.g., sea salt and organics), which is consistent with both modern [*de Leeuw et al*., 2011; *Quinn and Bates*, 2011] and classic PMA studies (reviewed by *Lewis and Schwartz* [2004]).

PMA contains sodium chloride, which is one of the most hygroscopic substances found in the atmosphere. As a result, PMA particles readily act as cloud condensation nuclei (CCN), with precise CCN behavior

determined by the chemical composition and size of individual PMA particles [*Collins et al*., 2013]. However, as the comparison of typical PMA and total marine aerosol number concentrations above suggests, PMA is apparently not the dominant contributor to total marine CCN, at least at high supersaturations (>0.5%). *Dinger et al*. [1970] found that nonvolatile particles (at 600°C) in clean marine air, which were interpreted as sea-salt particles, accounted for less than ~10% of total CCN numbers at 0.75% supersaturation over the North Atlantic Ocean southeast of Puerto Rico (this fraction decreased with altitude and reached zero at 2–3 km, the altitude of the inversion layer). *Hobbs* [1971] found that sodium-containing particles with $D_p$ in the range 0.06–0.68 μm accounted for only ~0.05–2% of total CCN numbers at 0.5% supersaturation measured during three aircraft flights off the coast of Seattle, Washington. Further studies suggested that, at 0.5% supersaturation, most marine CCN are likely formed or transported in the free troposphere and then entrained into the MBL [*Fitzgerald*, 1991; *Quinn and Bates*, 2011; *Clarke et al*., 2013].

Due to its high CCN activity, sea-salt aerosol should form greater fractions of total CCN at lower supersaturations (<0.5%) than it does at high supersaturations, because the competition among different particle types (e.g., sulfates and secondary organics) for available water vapor is tighter at low supersaturation [*Nenes et al*., 2001]. However, observational data supporting this statement are surprisingly scarce. In a recent study in the Southeast Pacific Ocean off the coast of Chile (as part of VOCALS-REx), *Blot et al*. [2013] estimated that PMA contributed approximately 20% of the total CCN active at 0.2–0.32% supersaturation. Additionally, high mass fractions of sea salt have been observed in the dried residuals of marine stratocumulus and cumulus cloud droplets (21–68%) over the northeastern Pacific and Indian Oceans, the Caribbean Sea, and the U.S. Midwest [*Twohy and Anderson*, 2008], and in residual particles larger than 0.2 μm in marine stratocumulus clouds (roughly 60–90%) off the coast of central California [*De Bock et al*., 2000]. These observations suggest that PMA was a major contributor to the CCN seeding the clouds on a mass basis. In the later study, particles larger than 0.2 μm diameter were seldom more than 10–20% of the total number of residual particles [*Noone et al*., 2000a, 2000b], which suggests salt particles contributed to a minimum of approximately 6–18% of the cloud droplet nuclei. An observation-based investigation of PMA CCN fractions as a function of supersaturation is required to better constrain estimates of the contribution of PMA to CCN budgets in different atmospheric environments.

PMA-driven increases in available CCN do not always translate proportionally into increases in cloud droplet number concentrations (CDNC). Bursting bubbles also produce coarse, supermicrometer particles (particularly via jet droplet production), and the PMA size distribution can extend up to tens of micrometers in diameter [*Lewis and Schwartz*, 2004]. Although they are few, coarse PMA particles have a large surface area and rapidly take up water, potentially reducing maximum cloud supersaturations. Under polluted conditions, this process can prevent large numbers of smaller and/or less hygroscopic particles from acting as CCN, and thereby lead to net decreases in cloud droplet number concentrations (CDNC) and increases in cloud droplet sizes and precipitation probabilities. These PMA-cloud interactions have been predicted by models [*Ghan et al*., 1998; *Karydis et al*., 2012] and identified in satellite observations [*Rosenfeld et al*., 2002; *Rudich et al*., 2002] but not yet observed in field measurements.

The aim of this study is to investigate PMA-cloud interactions off the coast of California through measurement of the contribution of PMA to CCN as a function of supersaturation, the direct detection of sea salt in cloud droplets, and comparison of collocated PMA and cloud microphysical measurements. The study is based on marine aerosol, CCN, and cloud measurements from the Eastern Pacific Emitted Aerosol Cloud Experiment (E-PEACE), which was conducted off the Central Coast of California in July and August 2011 [*Russell et al*., 2013], and the Stratocumulus Observations of Los-Angeles Emissions Derived Aerosol-Droplets (SOLEDAD) field study, which was conducted in La Jolla, Southern California, in May and June 2012 [*Zhao et al*., 2014; *Schroder et al*., 2015].

In section 2 the field studies are described in detail, including the experimental methods and instrumentation employed. Section 3 describes the data processing and analysis methods that were applied to the observational data. In particular, we introduce a new method for isolating PMA number size distributions from total particle size distributions through the use of a characteristic PMA modal size and shape. In section 4, this method is applied to E-PEACE PMA observations. Chemical measurements are used to verify

that the method provides reliable estimates of PMA number concentrations. Then, these number concentrations, direct measurements of sea-salt mass concentrations in cloud droplet residuals from the SOLEDAD campaign, and cloud supersaturation measurements are used to evaluate the role of PMA in nucleating cloud droplets for the clouds sampled during E-PEACE and SOLEDAD. Finally, section 4.4 is an investigation of the effects of PMA on cloud droplet number concentrations. The overall conclusions of the study are outlined in section 5.

## 2. Measurements

### 2.1. E-PEACE

#### 2.1.1. General Description

E-PEACE was an integrated ship cruise, aircraft, satellite, and modeling study conducted off the coast of Monterey, California, in July and August 2011. *Russell et al*. [2013] provide a full overview of the campaign. A full payload of instruments was employed across the ship and aircraft platforms to characterize particle and cloud number, mass, and composition (see Table 3 of *Russell et al*. [2013]) in background conditions and while modified by ship-emitted particle plumes. This study focuses on PMA, a natural source of aerosol, and only uses E-PEACE background data that have been filtered of any time periods influenced by the ship-emitted aerosol types.

The E-PEACE cruise took place on the R/V *Point Sur*, which sailed out of Monterey, California, for 12 days from 12 to 23 July 2011. Aerosol instruments were housed in a modified shipping container ($2.7 \times 2.1 \times 2$ m, length × width × height) secured on the bow of the R/V *Point Sur*. A common inlet (aluminum, ID 1.5″, OD 1.125″, length 2.4 m) drew air from 7.6 m above sea level into the container at 51 Lpm. A rain hat was installed at the top of the inlet to prevent the sampling of rain and large spray drops.

The E-PEACE aircraft measurements were carried out by the Center for Interdisciplinary Remotely-Piloted Aircraft Studies (CIRPAS) Twin Otter, which completed 30 flights out of Marina, California, from 8 July to 18 August 2011. Some of these flights were coordinated with the R/V *Point Sur* to measure cloud perturbations caused by the smoke plumes purposely emitted from the stern of the ship [see *Russell et al*., 2013], while others were directed at the plumes of large container ships passing through the study area. In this study, we primarily use the considerable amount of background cloud data that was collected as the Twin Otter flew between different emitted aerosol plumes and its base airport. The general study area covered by both ship and aircraft platforms during E-PEACE extended from 35.9° to 37.2°N and 121.8°–124.5°E.

#### 2.1.2. Shipboard Measurements

Dry particle size distributions were measured over the diameter range 0.01–20 μm with a Scanning Electrical Mobility Spectrometer (SEMS 0.01–1 μm $D_p$; Brechtel Manufacturing Incorporated (BMI), Hayward, California, model 2002, BMI model 2000C differential mobility analyzer (DMA), and TSI model 3781 condensation particle counter (CPC)), an Optical Particle Sizer (OPS 0.3–10 μm $D_p$; TSI, Shoreview, Minnesota, model 3330), and an Aerodynamic Particle Sizer (APS 0.5–20 μm $D_p$; TSI, Shoreview, Minnesota, model 3321). Diffusion driers were used upstream of each instrument to dry the ambient aerosol. Relative humidity in the SEMS ranged from 13 to 29%. Sampling times for each size distribution were 5 min for the SEMS and 1 min for the OPS and APS.

Cloud condensation nuclei (CCN) concentrations were measured with a miniaturized version of the CCN counter (mCCNc) described by *Roberts and Nenes* [2005]. The mCCNc scanned over the supersaturation range 0.07 to 0.88% every 10 min. For each scan, the processed data were collected into supersaturation bins of width 0.05% (except for the first and last bins, which covered 0.07–0.1% and 0.85–0.88%, respectively). Size-resolved subsaturated hygroscopic growth was measured with a Humidified Tandem Differential Mobility Analyzer (HTDMA, model 3002, Brechtel Manufacturing Incorporated (BMI), Hayward, California). The HTDMA measured Hygroscopic Growth Factors (HGF) of particles with initial dry diameters of 30, 75, and 150 nm at RHs of 40, 70, 85, and 92%. Further details of the instrument, including the data processing and quality control measures that were applied, are provided by *Wonaschütz et al*. [2013].

Dried submicrometer particles were collected on 37 mm Teflon filters for offline analysis of total organic mass and organic functional group concentrations by Fourier transform infrared (FTIR) spectroscopy [*Russell et al*., 2009; *Takahama et al*., 2013], and inorganic ion concentrations for elements heavier than Na by X-ray

fluorescence (XRF) spectroscopy (Chester LabNet, Tigard, Oregon). Sample collection time on the filters ranged from 3 to 8.9 h and averaged 5.4 h. *Frossard and Russell* [2012] present further details of the FTIR analysis, including description of the dehydration procedure necessary to remove hydrated water from PMA-influenced samples.

Nonrefractory, submicrometer chemical composition was measured online with a high-resolution time-of-flight aerosol mass spectrometer (HR-AMS, Aerodyne Research, Inc.) [*DeCarlo et al*., 2006]. A collection efficiency of 1 was applied based on comparison of HR-AMS and XRF sulfate concentrations, and total HR-AMS and particle size distribution-derived mass concentrations (Figure S1 in the supporting information). The HR-AMS was also used to measure sea salt, a refractory chemical component, with further details provided in section S4 in the supporting information. The HR-AMS vaporizer was operated at a temperature of 600°C. Black carbon (BC) concentrations were measured with a single particle soot photometer (SP2, 8 channel version, Droplet Measurement Technologies, Boulder, Colorado).

Standard weather parameters including air temperature, true wind speed and direction, and incident solar radiation were measured from the ship's mast.

#### 2.1.3. Aircraft Measurements

Cloud droplet size distributions and concentrations were measured with a Cloud and Aerosol Spectrometer (0.65–55 μm) (Droplet Measurement Technologies, Boulder, Colorado). Aerosol particle size distributions (0.1–3 μm) were measured with a Passive Cavity Aerosol Spectrometer Probe (Droplet Measurement Technologies, Boulder, Colorado) mounted under the wing of the Twin Otter. Cloud liquid water content (LWC) was measured by a PVM-100 probe (Gerber Scientific, Inc., Reston, Virginia).

Cloud droplet residuals were sampled with a Counterflow Virtual Impactor (CVI) inlet. Full details of the inlet are provided by *Shingler et al*. [2012]. CCN concentrations of cloud droplet residual particles were measured with a Droplet Measurement Technologies streamwise thermal-gradient cloud condensation nuclei counter [*Roberts and Nenes*, 2005]. The instrument was operated in scanning flow CCN analysis mode [*Moore and Nenes*, 2009]. CCN spectra over the supersaturation range 0.15–0.85% were produced at a time resolution of 40 s. Further details of the instrument operation and data processing steps are provided in section S2 in the supporting information.

Cloud water samples were collected with a modified Mohnen slotted cloud water collector [*Hegg and Hobbs*, 1986], treated with chloroform to minimize biological processing, stored at 5°C and analyzed offline by inductively coupled plasma–mass spectrometry and ion chromatography (IC). *Sorooshian et al*. [2013] and *Wang et al*. [2014] provide full details of the analytical procedures.

### 2.2. SOLEDAD

#### 2.2.1. General Description

The SOLEDAD field campaign was conducted at two sites in the Southern Californian coastal town of La Jolla in May and June 2012. The primary site was situated on Mount Soledad (32.84°N, 117.25°W) at an elevation of 251 m (asl) and a distance of 2–3 km from the coast (depending on direction). Low-level clouds are common in La Jolla during this time of year. At night, the cloud base often descends to below the sampling site, which created periods during the campaign when the Mount Soledad site was in-cloud for prolonged amounts of time (~10 h). Instrumentation was housed in a modified shipping container equipped with an inlet designed for aerosol sampling [*Bates et al*., 2002].

A Counterflow Virtual Impactor (CVI) inlet [*Noone et al*., 1988] was mounted on the container roof for sampling cloud droplet residual particles during the periods when the site was in cloud. The CVI inlet used a wind tunnel to accelerate droplets to impaction velocity. Extensive details of the CVI inlet and its operation and performance in SOLEDAD can be found in *Schroder et al*. [2015] and section S1 in the supporting information.

The primary field site was in-cloud a total of 8 times during the Soledad study period. The CVI inlet and the instruments relevant to this study were working simultaneously for three of these events, which we designate Cloud 1 (23:50 31 May 2012–09:30 1 June 2012), Cloud 2 (22:00 12 June 2012–11:35 13 June 2012), and Cloud 3 (20:00 17 June 2012–08:15 18 June 2012).

The secondary SOLEDAD field site was located in an enclosure at the end of Scripps Pier at Scripps Institution of Oceanography (inlet height 13 m asl). The straight line distance to the elevated field site on Mount Soledad is 3 km. The purpose of the pier sampling was to investigate properties of the below-cloud aerosol and to

compare with equivalent measurements taken at the primary Mount Soledad site further inland. No in-cloud sampling was conducted at the Scripps Pier site.

#### 2.2.2. Mount Soledad Measurements

Comprehensive measurements of physical and chemical aerosol, cloud, and trace gas properties were conducted for SOLEDAD. Here we discuss only the measurements relevant to this study. Further details of other instrumentation deployed can be found in *Schroder et al*. [2015] and *Zhao et al*. [2014].

Dry aerosol particle size distributions were measured over the diameter range 0.01–20 μm with the same identical instruments deployed for this purpose on the R/V *Point Sur* during E-PEACE.

CCN concentrations were measured with two mCCNc counters of the *Roberts and Nenes* [2005] design. One counter scanned over the supersaturation range 0.1–0.74% every 10 min. The other counter measured CCN concentrations at a constant supersaturation of 0.3%. The counters sampled in parallel from the aerosol inlet during cloud-free periods and from the CVI inlet during the in-cloud sampling periods.

Cloud droplet number concentrations and size distributions over the range 2–50 μm diameter were measured at 1 s resolution with an optical spectrometer (Fog Monitor model FM-100, Droplet Measurement Technologies, Boulder, Colorado). Specific details can be found in *Schroder et al*. [2015].

The mass concentrations of nonrefractory chemical species and sea salt (section S4 in the supporting information) in submicrometer aerosol particles and cloud droplet residuals were measured with the same HR-AMS (Aerodyne Research, Inc.) [*DeCarlo et al*., 2006] deployed on the E-PEACE ship cruise. However, a different collection efficiency of 0.6 was applied to the SOLEDAD data based on comparison of HR-AMS and IC sulfate concentrations, and total HR-AMS and particle size distribution-derived mass concentrations (Figure S2 in the supporting information). The HR-AMS sampled ambient particles from the total inlet during cloud-free periods and cloud droplet residuals from the CVI inlet during the in-cloud sampling periods (the same collection efficiency was applied for aerosol and residual particles). Care must be taken when calculating absolute concentrations measured by the CVI-HR-AMS system to take account of the imperfect sampling of cloud droplets by the CVI. These issues are described in detail in section S1 in the supporting information.

Black carbon (BC) concentrations were measured with a single particle soot photometer (SP2, eight-channel version, Droplet Measurement Technologies, Boulder, Colorado). Extensive details can be found in *Schroder et al*. [2015].

Dried submicrometer particles were sampled by the total inlet and collected on 37 mm Teflon filters. The filters were analyzed offline by IC [*Toom-Sauntry and Barrie*, 2002]. No filter samples were collected behind the CVI inlet due to the limited flow rate available.

Cloud water samples were collected over periods ranging from 3.8 to 11.6 h with a Caltech Active Strand Cloudwater Collecter Version 2 and analyzed for all major ions by IC [*Toom-Sauntry and Barrie*, 2002].

#### 2.2.3. Scripps Pier Measurements

At the Scripps Pier site, dry aerosol particle size distributions were measured over the diameter range 0.01–20 μm with a custom-built scanning DMA consisting of a TSI 3081 long column and TSI model 3010 CPC, and an Aerodynamic Particle Sizer (APS 0.5–20 μm $D_p$; TSI, Shoreview, Minnesota, model 3321). Dried submicrometer particles were collected on 37 mm Teflon filters, and inorganic ion concentrations were measured offline by IC [*Toom-Sauntry and Barrie*, 2002].

## 3. Data Analysis

### 3.1. Total Aerosol Size Distributions

Hourly-averaged scanning mobility particle sizer (SMPS), OPS, and APS measured size distributions were merged to generate total aerosol size distributions over the diameter range 0.01–20 μm. These instruments each use a different operating principle to size aerosol particles, which needs to be taken into account in the data merging procedure. The algorithm used here was based on the SMPS-APS combination procedure described by *Khlystov et al*. [2004] with additional steps added to take advantage of the large overlap region between the SMPS and OPS size distributions, when OPS data were available. Full details can be found in section S3 in the supporting information.

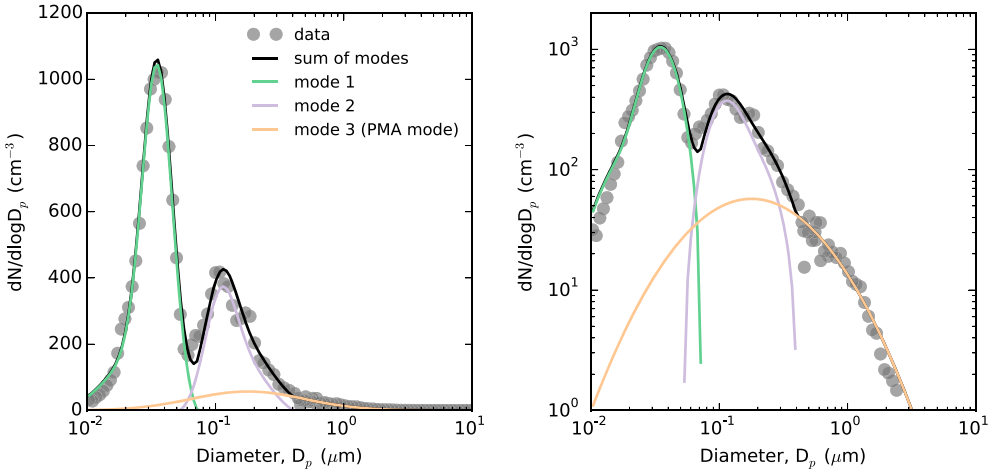


**Figure 1.** An example particle size distribution including fitted lognormal modes displayed on (left) linear and (right) log *y* axes. The distribution was measured from the R/V *Point Sur* at 0700 on 22 July 2011 during the E-PEACE campaign. Mode 3 represents the PMA mode (see sections 3.2 and 4.1.2 in the main text).

### 3.2. PMA-Mode-Fitting Procedure

Multiple lognormal modes were fit to the hourly-averaged total marine aerosol size distributions using a constrained nonlinear optimization algorithm implemented in the Matlab software package (based on the fmincon function). We used lognormal functions of the form

$$N_i(D_p) = \frac{N_{t,i}}{\sqrt{2\pi}\log_{10}\sigma_{g,i}} e^{-\frac{(\log_{10} D_p - \log_{10}\mu_i)^2}{2(\log_{10}\sigma_{g,i})^2}} \quad (1)$$

where $N_{t,i}$ represents the total number concentration, $\mu_i$ the mean diameter, and $\sigma_{g,i}$ the geometric standard deviation of mode *i*.

Motivated by the appearance of a broad shoulder in the total aerosol size distributions at $D_p > 0.5$ μm at high wind speeds (discussed below in section 4.1.1), a mode-fitting procedure was devised to isolate a PMA mode from the set of fitted lognormal modes for each size distribution. The first mode fitted to each size distribution was constrained to have a mean diameter of 0.2 μm ± 30% (0.14–0.26 μm) and geometric standard deviation between 2.5 and 3, and it was fitted to only the upper portion of each size distribution ($D_p > 0.5$ μm). Constraining the parameters of the mode in this manner ensured that its shape was comparable to the shape of the breaking wave PMA size distribution recently measured in the Scripps wave channel [*Prather et al.*, 2013] and, at diameters greater than 0.1 μm, the shape of the canonical PMA size distribution defined by *Lewis and Schwartz* [2004]. These choices are discussed in detail below.

The remaining lognormal modes were fit to the residual size distributions following subtraction of the PMA mode. These modes were allowed to have any mean diameter over the measured size range, but they were forced to have geometric standard deviations less than 2, consistent with typical submicrometer aerosol size modes [*Heintzenberg et al.*, 2000; *Seinfeld and Pandis*, 2006]. The number of modes fit to each residual size distribution was the minimum number of modes required to achieve a size distribution reconstruction error of less than 10%. This rule resulted in two to four modes being fit to the residual particle size distributions.

The fitting results, including the PMA mode, were grouped into three particle size distribution (PSD) modes for further analysis: PSD mode 1 had mean diameter in the range 25–80 nm and represents the Aitken mode, PSD mode 2 had mean diameter in the range 100–200 nm and represents the cloud-processed accumulation mode, and PSD mode 3 is the PMA mode. A characteristic example size distribution from E-PEACE and the three PSD modes resulting from the fitting and classification procedure are shown in Figure 1.

We suggest that a single broad mode is a good approximation of PMA number size distributions [*Lewis and Schwartz*, 2004; *Bates et al.*, 2012; *Prather et al.*, 2013], which are most likely formed from the combination of a number of narrower overlapping modes [*Modini et al.*, 2013], each of which may be composed of particles

with different chemical compositions. This approach is similar to that of *Collins et al.* [2013] who argued that the broad size distribution of PMA particles observed in the Scripps wave channel [*Prather et al.*, 2013] resulted from the combination of three narrower overlapping lognormal modes, each containing particles of different composition: the mode with the smallest mean diameter ($D_p < 0.1$ μm) contained pure organic particles, while the two remaining modes contained internally mixed sea-salt organic particles.

The most important source of potential error in this approximation is the possibility that the assumed shape of the PMA mode does not match the shape of the size distribution of real PMA particles in the marine atmosphere. This error would result in PMA particles being misclassified as mode 1 or 2 particles, or vice versa. For example, an additional mode of particles with $D_p < 20$ nm has been observed in one experiment in the Scripps wave channel [*Prather et al.*, 2013, Figure 1b] (the lower tail of the size distribution does not approach zero) but not others [*Stokes et al.*, 2013]. This potential error would affect the number concentrations calculated from the PMA mode fits (section 4.1.1) but not the PMA contributions to CCN (section 4.1.3), since particles with diameters less than 20 nm are too small to activate at supersaturations less than 0.88%.

Nonrepresentative PMA size distributions could also arise from placing incorrect constraints on the PMA modal parameters. To get a sense of the potential consequences of this error, the sensitivity of the integrated number concentrations in the fitted PMA modes to the constraints placed on the PMA modal parameters is explored in Figure S3. If the range of allowable PMA mean diameters ($\mu_{PMA}$) is decreased to 0.105–0.195 μm, the amplitudes of the fitted PMA modes increase, and the number concentrations of particles in the modes increase by an average of 28 ± 22% (1 standard deviation). If the range of allowable mean diameters is increased to 0.175–0.325 μm, integrated number concentrations decrease by 10 ± 12%. The assumed width of the PMA mode is also important. Narrowing the range of allowable geometric standard deviations ($\sigma_{g,PMA}$) to 2–2.5 decreases number concentrations by 9 ± 25%.

Given this sensitivity, the functional form and constraints were chosen to be consistent with the single, broad lognormal mode in the canonical size distribution derived by *Lewis and Schwartz* [2004] from their extensive review of ambient size distribution measurements. Further analysis in section 4.1.2 supports this choice for the representation of the PMA size distribution.

### 3.3. Calculation of Nonsea-Salt (nss) Sulfate and Sea-Salt Mass Concentrations

Sea-salt mass concentrations in aerosol (XRF and IC) and cloud water (IC) samples were calculated as the sum of $Cl^-$ and $1.47 \times Na^+$ mass concentrations, following *Bates et al.* [2008]. The factor of 1.47 accounts for the contribution of $K^+$, $Mg^{+2}$, $Ca^{+2}$, $SO_4^{-2}$, and $HCO_3^-$ to sea salt, and the dependence on $Cl^-$ concentration means the calculation explicitly takes chloride depletion into account. Sea-salt mass concentrations were estimated from HR-AMS measurements following a procedure similar to that outlined by *Ovadnevaite et al.* [2012]. Full details of this procedure are described in section S4 in the supporting information. Non-sea-salt (nss) sulfate mass concentrations were calculated by subtracting sea-salt sulfate from total sulfate concentrations separately for the XRF, IC, and HR-AMS data. Sea-salt sulfate was calculated from total sea-salt concentrations and the ratio of sodium to total salt concentration in seawater [*Lewis and Schwartz*, 2004]. XRF sulfate concentrations were calculated from XRF sulfur ion measurements assuming that all the sulfur was present as sulfate.

## 4. Results and Discussion

### 4.1. PMA Observations—E-PEACE

#### 4.1.1. PMA Number Concentrations

The time series of submicrometer sea-salt mass concentrations over the E-PEACE ship cruise period is shown in Figure 2. Surface wind speed and particle number size distributions are also plotted. The study period can be split into two distinct periods, which are separated by the dashed vertical line in Figure 2. During the first week of the campaign from 12 to 20 July, wind speeds were generally lower, averaging 11.9 ± 0.3 m $s^{-1}$ (±1 standard error of the mean), and sea-salt mass concentrations were generally less than 0.2 μg $m^{-3}$ (average 0.14 ± 0.01 μg $m^{-3}$). During the second part of the cruise from 20 to 24 July, wind speeds increased to an average of 15.9 ± 0.6 m $s^{-1}$. The sea state was generally rougher, and more frequent whitecap formation was observed. Sea-salt concentrations increased simultaneously to an average of 0.58 ± 0.01 μg $m^{-3}$. Coincident

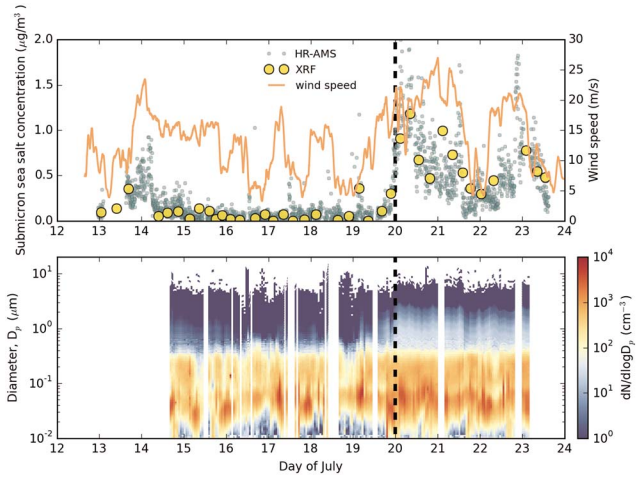


**Figure 2.** Time series of submicrometer sea-salt mass concentrations measured by XRF and HR-AMS, wind speed, and total aerosol size distributions (image plot of $dN/d\log D_p$ concentrations) over the E-PEACE ship cruise period. The dashed vertical line separates the low-PMA period from 12 to 20 July and the high-PMA period from 20 to 24 July.

with this shift in conditions on 20 July and the strong increase in submicrometer sea-salt mass concentrations, there was a distinct change in the shape of the particle number size distributions. The concentrations of larger submicrometer particles increased as indicated by the appearance of a shoulder in the particle size distributions above 500 nm diameter (Figure 2).

The relationship between large submicrometer particle number concentration and submicrometer sea-salt mass concentration measured by HR-AMS and XRF is explicitly shown in Figure 3. The SOLEDAD measurements are also plotted and will be discussed later in section 4.2. Large submicrometer particle number concentration is defined as the integrated particle number concentration above 500 nm diameter. This cutoff was chosen to be above the size range of the accumulation mode identified in both the E-PEACE and SOLEDAD size distributions. For the E-PEACE measurements, a strong correlation was observed between the number of large submicrometer particles and sea-salt mass ($r = 0.86$, $n = 173$ for HR-AMS sea salt; $r = 0.92$, $n = 33$ for XRF sea salt). This strongly suggests that the broad shoulder in the E-PEACE size distributions above 500 nm diameter belonged to a PMA mode.

Motivated by this result, a lognormal mode with mean diameter and geometric standard deviation constrained to agree with measured PMA size distributions [*Lewis and Schwartz*, 2004; *Prather et al.*, 2013] was fit to the particle size distributions, and then modes were fit to the residual size distributions remaining after subtraction of the PMA mode (section 3.2). A PMA mode was fit to 76% of the size distributions. In the remaining 24% of cases, the PMA mode fit failed because the concentrations of particles with diameter larger than 500 nm were too small or appeared to contain contributions from other sources. These cases were removed from further analysis.

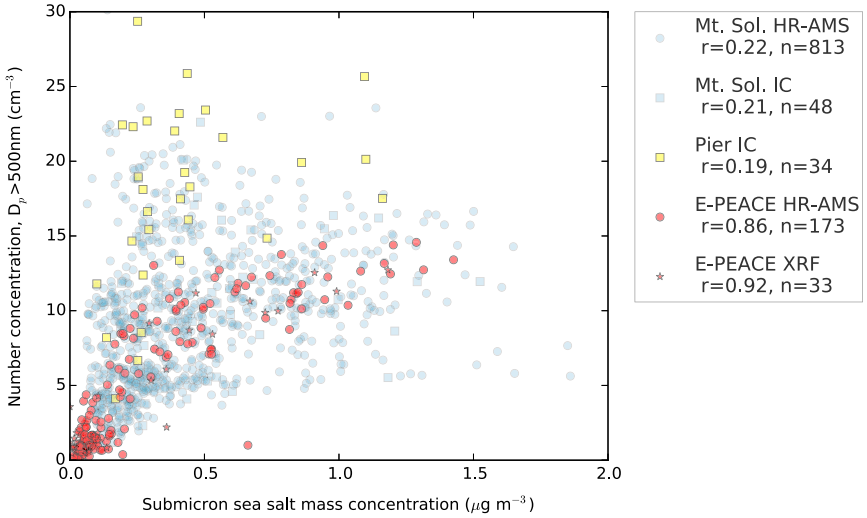


**Figure 3.** Large particle number concentrations ($D_p > 500$ nm) versus submicrometer sea-salt mass concentrations measured by HR-AMS, IC, and XRF for both of the SOLEDAD field sites (Mount Soledad and Scripps Pier) and the E-PEACE ship cruise. Pearson correlation coefficients ($r$) are displayed with sample sizes ($n$) in the legend.

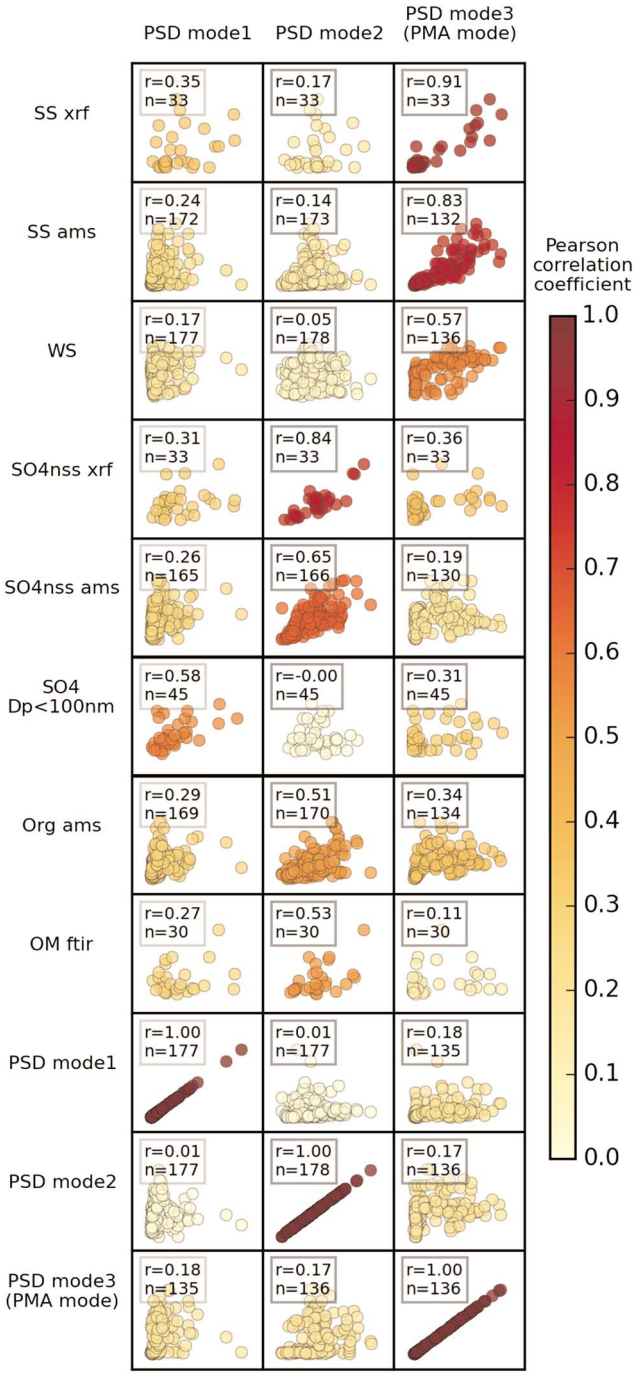


**Figure 4.** Scatterplots of the integrated mass concentrations of particles in each PSD mode and different chemical species, wind speed, and the mass concentrations of particles in the other PSD modes for E-PEACE ship cruise data. Each plot is colored by the Pearson correlation coefficient between its two variables. The Pearson correlation coefficients are also displayed in the upper left corner of each plot ($r$) with sample sizes ($n$). "SS" means sea salt, "xrf" concentrations measured by XRF, "ams" concentrations measured by HR-AMS, and "ftir" concentrations measured by FTIR spectroscopy.

The combination of PSD modes 1 and 2 formed a bimodal marine aerosol size distribution that was present throughout the entire E-PEACE cruise (Figure 2). PSD mode 3 only appeared episodically during periods of higher wind speed. The hourly-averaged, integrated number concentration of PSD mode 3, which we take to represent PMA number concentration, varied from 3 to 103 $cm^{-3}$. The average number concentration (±1 standard error of the mean) was $12 \pm 2\,cm^{-3}$ during the low-PMA period (12 to 20 July) and $71 \pm 2\,cm^{-3}$ during the high-PMA period (20–24 July).

#### 4.1.2. Identification of Particle Size Distribution Modes

To test how well PSD mode 3 approximates the PMA size distribution and to explore possible species assignments for the other PSD modes, the correlation between the integrated mass concentration of particles in each PSD mode (calculated assuming density of 1 g $cm^{-3}$ since only relative changes were assessed) and the mass concentrations of key chemical species, wind speed, and the mass concentration of particles in each of the other PSD modes is shown in Figure 4. PSD mode mass concentrations were used in this analysis because they relate more directly to mass concentrations of chemical species than particle number concentrations. If the integrated number concentrations of particles in each PSD mode are used in the analysis, a similar overall picture emerges with some differences that are explained further below (Figure S4 in the supporting information).

The mass concentration of particles in PSD mode 3 correlated strongly ($r>0.75$) with sea-salt mass concentration measured by XRF ($r=0.91$, $n=33$) and HR-AMS ($r=0.83$, $n=132$), and moderately ($r>0.5$) with wind speed ($r=0.57$, $n=136$). This supports our assignment of PMA to this particle mode and confirms our assertion that it is a reasonable approximation to the PMA number size distribution.

The mass concentration of particles in PSD mode 2 correlated strongly or moderately

with nss sulfate (XRF $r = 0.84$, $n = 33$; AMS $r = 0.65$, $n = 166$), which suggests nss sulfate was the controlling chemical component of the accumulation mode.

The mass concentration of particles in PSD mode 1 correlated moderately with sulfate mass concentrations for particles with diameter less than 100 nm ($r = 0.58$, $n = 45$), which was calculated from the HR-AMS sulfate Particle time-of-flight (PToF) size distributions. The number concentration of particles in PSD mode 1 correlated only weakly with sub-100 nm nss sulfate (Figure S4). However, a further observation of interest is that sulfate was the only chemical component for which a sub-100 nm concentration signal could be discerned above random measurement error, which becomes important at small particle sizes in the HR-AMS. The first-order autocorrelation coefficient for hourly-averaged sub-100 nm $SO_4$ mass concentrations was 0.34 ($N = 104$), significantly greater than 0 at the 95% confidence level, indicating that each measurement point had some dependence on the value preceding it, which is expected for an hourly-resolved time series of background aerosol concentrations. As a counter example, the first-order autocorrelation coefficient of sub-100 nm organic mass concentrations was 0.04, which indicated that any sub-100 nm organic signal was dominated by random measurement error (consequently, correlation between PSD mode 1 concentrations and sub-100 nm organic concentrations was poor on both a mass ($r = -0.01$, $n = 45$) and number ($r = 0.21$, $n = 45$) basis). The fact that sulfate was the only nonrefractory species measured by HR-AMS for which a clear sub-100 nm signal could be derived, combined with the moderate correlation observed with the corresponding mass concentrations (Figure 4), suggests that nss sulfate was the major chemical component of the Aitken mode (mode 1).

Only weak to moderate correlations were observed between organic aerosol mass concentrations (measured by HR-AMS and FTIR) and each PSD mode, suggesting that organic components contributed mass to each mode, but likely not as much mass as nss sulfate contributed to PSD modes 1 and 2 and sea salt contributed to the PMA mode. The organic mass concentrations measured by HR-AMS and FTIR correlated poorly with both sea-salt mass concentrations and wind speed (Figures S5 and S6 in the supporting information), which suggests that the majority of the organic mass had non-PMA origins. This finding is consistent with *Frossard et al.* [2014] who showed that many of the E-PEACE organic measurements included both PMA-associated and shipping or coastal organic components.

These chemical assignments are consistent with HTDMA measured Hygroscopic Growth Factors (HGF). Campaign average HGF at 92% RH were 1.41, 1.49, and 1.55 for particles with diameter 30, 75, and 150 nm, respectively. These growth factors are consistent with the hygroscopic behavior of internally mixed sulfate-organic particles [*Swietlicki et al.*, 2008].

Weak correlation was observed between each of the three PSD modes on a mass ($r = 0.01$–$0.18$, $n = 135$–$178$; Figure 4) and number basis ($r = 0.30$–$0.44$, $n = 136$–$178$; Figure S4 in the supporting information), suggesting that the lognormal-mode-fitting procedure was effective in separating the particle size distributions into modes that arose from different, uncorrelated production processes.

Overall, these correlation results (Figures 4 and S4) support the assumptions behind the PMA-mode-fitting procedure detailed in section 3.2. The observations suggest that PSD modes 1 and 2 did not include substantial PMA contributions and that single, broad lognormal modes effectively represented the number size distributions of ambient PMA particles in E-PEACE.

#### 4.1.3. Contribution of PMA to CCN

Collocated with the PMA number size distribution measurements, CCN spectra were measured from the R/V *Point Sur* during E-PEACE. Figure 5a displays measured CCN concentrations ($N_{CCN}$) as a function of supersaturation. CCN concentration increased steadily with increasing supersaturation. In the lowest supersaturation bin, 0.07–0.1%, CCN concentrations averaged 153 $cm^{-3}$. The corresponding value for supersaturation bin 0.85–0.88% was 553 $cm^{-3}$, which indicates more than half of the total aerosol activated at this supersaturation, since background particle number concentrations averaged 816 $cm^{-3}$ throughout the study period.

The coefficients of correlation between the number concentration of particles in each PSD mode and CCN concentrations are plotted in Figure 5b. At lower supersaturation, PSD mode 2 and the PMA mode correlated strongly with CCN. The correlation coefficient between $N_{CCN}$ and the combined number concentration of particles in mode 2 and the PMA mode was 0.85 ($n = 99$). Additionally, very weak

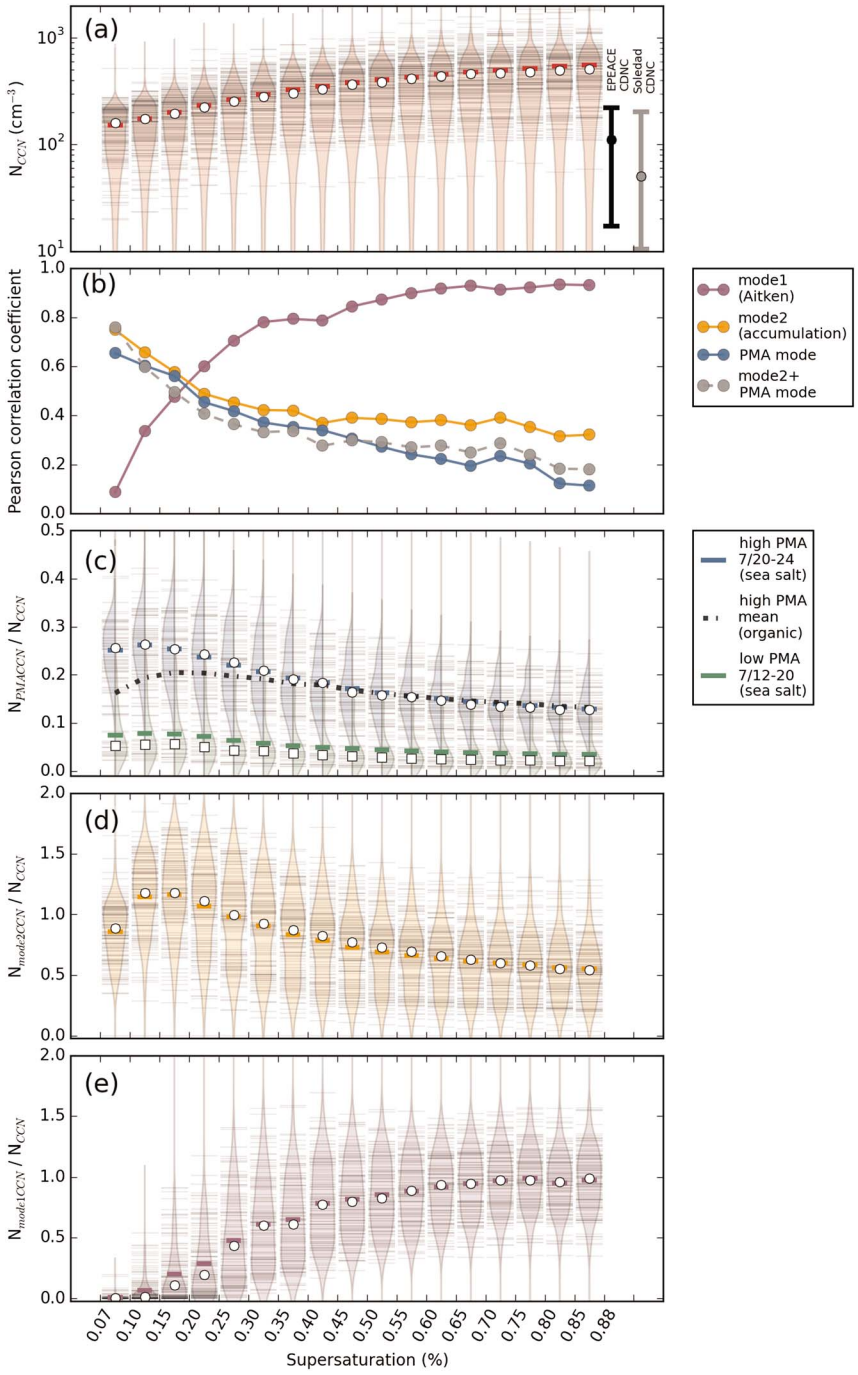


**Figure 5.** (a) Beanplots of CCN concentrations as a function of supersaturation measured from the R/V *Point Sur* during E-PEACE. The light grey horizontal bars represent all of the hourly average observations at a given supersaturation taken during the entire campaign, the pink violin bodies are Kernel Density Estimates of the probability density functions of the observations, the pink solid line through each violin body is the mean, and the white circle marker is the median of all observations taken at a particular supersaturation. The vertical capped bars with circle markers represent the range (1st–99th percentile) and median of cloud droplet number concentrations measured during E-PEACE (black) and SOLEDAD (grey) (b) The Pearson coefficients of correlation between CCN concentrations and the number concentration of particles in each PSD mode as a function of supersaturation ($n$ = 131 for each coefficient) (c–e) Beanplots of the fractional contribution CCN active particles in each particle mode to total CCN number concentrations ($N_{\text{modeX CCN}}/N_{\text{CCN}}$). The dashed-dotted black line in Figure 5c is the mean contribution of PMA to CCN predicted under the assumption that the PMA particles are completely organic. The splitting of the violins in Figure 5c is explained further in the main text.

correlation was observed between PSD mode 1 and CCN ($r = 0.09$, $n = 131$). This suggests that the population of particles activating to cloud droplets at low supersaturation was mainly composed of particles from PSD mode 2 and the PMA mode.

As supersaturation and the absolute number of CCN increased, the correlation between $N_{CCN}$ and PSD modes 2 and the PMA mode weakened, while the correlation between $N_{CCN}$ and PSD mode 1 strengthened. This observation can be explained by the fact that more and more particles from the more abundant PSD mode 1 activated as supersaturation was increased in the CCN counter, while the numbers of activating particles from PSD mode 2 and the PMA mode stayed comparatively constant. Eventually, for the highest supersaturation obtained in the instrument 0.85–0.88%, PSD mode 1 correlated very strongly with CCN with $r = 0.92$ ($n = 131$). This high correlation suggests that changes in CCN concentration at high supersaturations can be attributed to changes in the concentration of PSD mode 1 particles.

The fractional contributions of CCN active particles in each PSD mode to total CCN ($N_{\text{mode}X\ CCN}/N_{CCN}$) are displayed in Figures 5c–5e. CCN active particles are defined as particles with diameter greater than the CCN activation diameter at a particular supersaturation. Calculation of the number of CCN active particles in a given PSD mode requires knowledge or assumption of the chemical composition of particles in that mode in order to determine activation diameters as a function of supersaturation.

The results discussed in section 4.1.2 suggest that nss sulfate was the dominant contributor to PSD modes 1 and 2, but that organic species likely also made up some fraction. Here we simply assume the particles were composed entirely of ammonium sulfate and calculate activation diameters as a function of supersaturation with the parameterization reported by *Koehler et al*. [2006]. Since the organic species present would have likely decreased the CCN activity of PSD modes 1 and 2 particles relative to pure sulfate particles, this assumption results in underestimation of the true activation diameters and, consequently, overprediction of the number of CCN active particles in these size modes. For PSD mode 2 alone, the mean fraction of CCN active particles to total CCN is calculated to be greater than 1 for supersaturations in the range 0.1–0.3%, which is clearly not possible. The assumed composition of particles in these size modes could be adjusted to achieve quantitative CCN closure. However, this problem is incompletely constrained, and as non-PMA particles are not the main focus of the study, we simply confine our discussion of the number of CCN active particles in PSD modes 1 and 2 to the trends observed with changing supersaturation in Figures 5d and 5e.

In contrast, the contributions of PMA CCN to total CCN concentrations are more accurately quantified in Figure 5c. The size-resolved chemical composition of PMA can vary substantially, and it was not measured in this study. Therefore, we consider the possible limit cases and bound the problem by considering what we classify as PMA to be either (a) completely inorganic sodium chloride (upper bound) or (b) completely organic (lower bound; modeled as fructose and/or glucose; saccharides are an important component of marine organic matter) [*Russell et al*., 2010] (see section S5 in the supporting information for further discussion). The lower bound assumption covers the possible presence of small ($D_p < 0.1\ \mu m$), less hygroscopic (compared to pure sea salt) organic PMA particles with effective hygroscopicity parameter around 0.2, even if contributions of non-PMA organic components (from shipping and coastal sources) meant that we could not identify the organic mass as wholly PMA (e.g., Figures S5 and S6). The actual contribution of PMA to CCN is expected to lie within the ranges formed by these two limit cases.

The contribution of PMA to CCN is examined separately in Figure 5c for the low (12 to 20 July, green, right half of the violin bodies) and high (20 to 24 July, blue, left half of the violin bodies) PMA periods identified in section 4.1.1 from Figure 2. On average during the high-PMA period, PMA contributed 24–28% of CCN at supersaturations less than 0.3%, assuming the PMA particles were composed completely of sea salt (range of individual observations 6–63%). The corresponding average contributions were 16–20% under the assumption that the PMA particles were composed completely of organics (range 5–48%). PMA made less of a contribution to CCN at higher supersaturations. For example at 0.85–0.88% supersaturation, the average contribution of PMA to CCN was 14% under the sea-salt assumption and 13% under the organic assumption (range 5–30% for both cases). The estimates become less sensitive to the assumed PMA composition as supersaturation increases since the predicted activation diameters decrease and move further out on the lower tail of the PMA mode. When determining contributions to CCN, chemical composition is only important for PMA particles activating at low supersaturations (which are common in marine stratocumulus clouds).

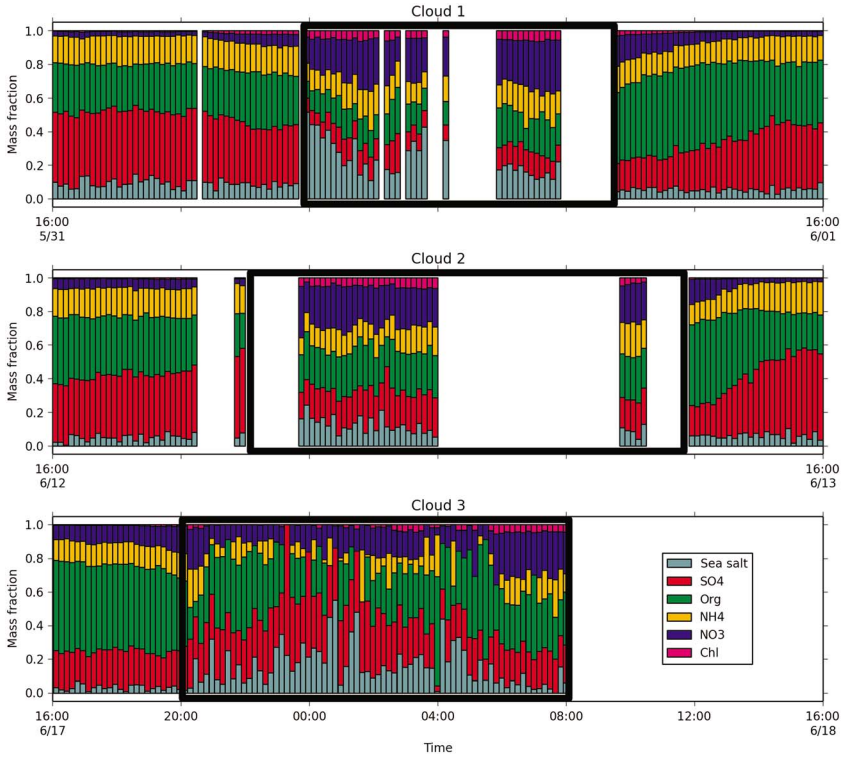


**Figure 6.** Relative mass fractions of chemical species measured by HR-AMS in dried cloud droplet residuals and in the aerosol particles sampled immediately before and after each cloud event at the Mt. Soledad site during SOLEDAD. The black windows designate the in-cloud periods when the HR-AMS sampled cloud droplet residuals through the CVI inlet.

The contributions of PMA to CCN were drastically lower during the low-PMA period. Even assuming the particles were completely composed of sea salt, it is estimated that on average PMA only contributed 5–10% of CCN particles at all supersaturations. This range decreases to 5–7% if it is assumed that the PMA particles were completely organic. It is noteworthy that total aerosol concentrations during this time period averaged only $664 \pm 45\ \mathrm{cm}^{-3}$ (± standard error of the mean). Therefore, even in clean marine conditions and at low supersaturations, if the ocean surface is relatively calm, PMA contributes very little to marine CCN number concentrations.

Examining the trends across the other PSD modes displayed in Figures 5d and 5e, at low supersaturation, particles from PSD mode 2 contributed strongly to total CCN, while PSD mode 1 particles contributed a much smaller fraction. As supersaturation was increased, the relative contribution from PSD mode 2 weakened, and that from PSD mode 1 strengthened. This supports the correlation results displayed in Figure 5b. The relative contribution of PMA to CCN was greatest at low supersaturation. PMA CCN fractions decreased with increasing supersaturation due to an increase in the number of activating Aitken mode particles.

### 4.2. Sea-Salt Observations—SOLEDAD

#### 4.2.1. Sea-Salt Concentrations

Submicrometer sea-salt mass concentrations in ambient aerosol sampled during the SOLEDAD field campaign ranged from 0.06 to $2.9\ \mu\mathrm{g\ m}^{-3}$ (AMS and IC) at the primary Mount Soledad field site and from 0.1 to $3\ \mu\mathrm{g\ m}^{-3}$ (IC only) at the secondary Scripps Pier site. These ranges are comparable to the range of sea-salt mass concentrations measured over the ocean from the R/V *Point Sur* during E-PEACE (Figures 2 and 3).

La Jolla is situated 16 km north of downtown San Diego and 80–200 km south of the South Coast Air Basin, which includes the counties of Los Angeles, Orange, Riverside, and San Bernardino, as well as the ports of Los Angeles and Long Beach. As a result, anthropogenic pollution influences were larger during the SOLEDAD project. For example, black carbon (BC) concentrations averaged $38 \pm 37\ \mathrm{ng\ m}^{-3}$ (±1 standard deviation)

at the Mount Soledad site, while corresponding background concentrations (i.e., when not sampling ship and other plumes) [*Russell et al*., 2013] for E-PEACE only averaged $1.8 \pm 2.1$ ng m$^{-3}$. Average total particle number concentrations were $1797 \pm 975$ cm$^{-3}$ at Mount Soledad compared to $816 \pm 471$ cm$^{-3}$ during E-PEACE. For reference, clean marine aerosol concentrations are typically 200–800 cm$^{-3}$ [*Fitzgerald*, 1991; *Heintzenberg et al*., 2000]

As a result of the multiple contributions from human activities (likely largely associated with northerly flow from the cities and ports of Los Angeles and Long Beach, [*Liu et al*., 2011], and with local sources from surrounding homes and vehicles), a more complex mixture of particle modes and chemical components was sampled during SOLEDAD than E-PEACE. Figure 3 shows that number concentrations of larger submicrometer particles were generally higher during SOLEDAD than during E-PEACE, particularly at low sea-salt concentrations. This indicates that there were likely sources of large particles other than PMA contributing to the SOLEDAD measurements. The enhanced concentrations (and large variability) prevented the detection of any relationship between the number concentration of particles with $D_p > 500$ nm and sea-salt mass concentration at either the Mount Soledad ($r = 0.21$–$0.22$) or Scripps Pier sites ($r = 0.19$). Consequently, the PMA-mode-fitting procedure introduced in section 3.2 could not be used to identify a PMA mode in total particle size distributions measured during SOLEDAD. This procedure can only be applied in conditions where the influence of particle sources other than PMA on the largest submicrometer mode is minimal.

#### 4.2.2. Sea-Salt Mass Fractions in Aerosol Particles and Cloud Droplets

Online measurements of sea salt in cloud droplets provided an alternative route for investigating the contribution of PMA to CCN and cloud formation. At the Mount Soledad site, sea-salt mass concentrations in the dried residuals of cloud droplets sampled with a CVI inlet were measured by HR-AMS. The CVI inlet and HR-AMS measured three cloud events (section 2.2.1). Submicrometer sea-salt mass concentrations in the residual particles of cloud droplets with diameters greater than 11.5 um (section S1 in the supporting information) were (mean ± 1 standard deviation) $0.30 \pm 0.16$ μg m$^{-3}$ for Cloud 1, $0.24 \pm 0.13$ μg m$^{-3}$ for Cloud 2, and $0.03 \pm 0.02$ μg m$^{-3}$ for Cloud 3. These observations indicate sea-salt-containing PMA particles contributed to the CCN seeding the clouds that impacted Mount Soledad.

The mass fractions of sea salt and the other chemical species typically measured by AMS ($SO_4$, Org, $NH_4$, $NO_3$, and Chl) in the cloud droplet residuals sampled during each of the three SOLEDAD cloud events are displayed in Figure 6 (AMS Chl represents the nonrefractory, nonsea-salt fraction of chloride, e.g., $NH_4Cl$ from anthropogenic sources) [*Salcedo et al*., 2006]. The mass fractions of the same chemical species in the aerosol particles sampled immediately before and after each cloud event are also displayed. The relative fractions of sea salt were greater in the cloud droplet residuals (mean ± 1 std. deviation, $24 \pm 12$% Cloud 1, $12 \pm 5$% Cloud 2, and $16 \pm 12$% Cloud 3) than in the aerosol particles sampled on either side of the cloud events ($7 \pm 3$% Cloud 1, $5 \pm 3$% Cloud 2, $3 \pm 1$% Cloud 3). This trend was also observed for nitrate.

The most likely reason for the higher fractions of sea salt in the cloud droplet residuals compared to the aerosol particles is that PMA particles activated into cloud droplets more readily than other particle types because of their relatively large sizes and higher hygroscopicity. However, at least part of the relative increase in sea salt could have been due to the evaporation of more volatile species as cloud droplets were dried to residual particles in the warm counterflow air of the CVI inlet (40°C). For example, gaseous isocyanic acid (HNCO) and nitric acid ($HNO_3$) were both observed by Chemical Ionization Mass Spectrometry (CIMS) behind the CVI inlet [*Zhao et al*., 2014]. Other volatile species not measured by CIMS during SOLEDAD may have also evaporated in the CVI inlet, thereby contributing to the relative increase in sea salt in the dried cloud droplet residuals.

Despite the possible evaporation of $HNO_3$ in the CVI inlet, the fractions of nitrate measured by HR-AMS were still greater in the cloud droplet residuals than in the aerosol particles. A part of this increase may have been due to the scavenging of ambient $HNO_3$ by the cloud droplets [*Hayden et al*., 2008]. Recent observations off the coast of California have shown that nucleation scavenging of nitrate-enhanced sea-salt particles (formed by chloride-depleting $HNO_3$ displacement reactions) also contributes to enhanced cloud water nitrate fractions [*Prabhakar et al*., 2014]. The $Cl^-$:$Na^+$ ratios in SOLEDAD cloud water samples were less than the corresponding ratio in seawater (1.2 in Cloud 1, 1.0 in Cloud 2, and 1.1 and 1.5 in Cloud 3 compared to 1.8 in seawater) [*Lewis and Schwartz*, 2004], which indicates that the SOLEDAD sea-salt CCN

were chloride depleted, likely at least partly due to $HNO_3$ displacement reactions that formed nitrate salts (e.g., $NaNO_3$ and $Mg(NO_3)_2$) in the sea-salt aerosol. Given that sea salt was found in greater proportions in the cloud droplet residuals than in the ambient aerosol particles, nitrate salt formation likely also contributed to the high-nitrate fractions observed in the cloud droplet residuals.

### 4.3. Comparison of E-PEACE and SOLEDAD Observations

#### 4.3.1. Cloud Types and Supersaturations

The E-PEACE and SOLEDAD projects both aimed to investigate aerosol interactions with low-level marine stratocumulus cloud that persistently cover large areas off the coast of California. Coverage peaks during the summer months June–August [*Iacobellis and Cayan*, 2013] and from 1950 to 1981 averaged 67% [*Klein and Hartmann*, 1993]. This section discusses the characteristics of the low-level clouds encountered during E-PEACE and SOLEDAD and presents measurements of cloud supersaturations, which are required to place the PMA results in context.

Only low supersaturations are expected to result from the shallow convection driving stratocumulus cloud formation and maintenance. Previous observations suggest stratocumulus supersaturations are typically less than 0.3% [*Hoppel et al*., 1986; *Leaitch et al*., 1996; *Roberts et al*., 2006] although there are some higher values reported when CCN concentrations are low and the rate of depletion of supersaturation in cloud is reduced [*Hudson et al*., 2010].

During E-PEACE, cloud top heights were typically below 700 m and cloud thicknesses ranged from 95 to 554 m [*Russell et al*., 2013]. Droplet number concentrations in clouds that were unperturbed by emitted particle sources (e.g., cargo ship exhaust, identified by the f99 signal measured by AMS) [see *Coggon et al*., 2012] ranged up to 463 $cm^{-3}$ but almost all values were below 222 $cm^{-3}$ (99th percentile). Figure 5a compares E-PEACE cloud droplet number concentrations (CDNC) to the CCN concentrations measured from the R/V *Point Sur*. The range of observed CDNC was broadly comparable to the concentrations of CCN active at supersaturations less than 0.1%, which suggests cloud supersaturations were generally low during E-PEACE.

Supersaturations in the E-PEACE stratocumulus clouds were also derived from measurements of the CCN spectra (40 s resolution) of cloud droplet residuals sampled behind the CVI inlet on the CIRPAS Twin Otter. Details are provided in section S2 in the supporting information. In some spectra, activation ratios of 1 were observed at all supersaturations in the CCN counter, which indicates the residual particles activated below the lowest supersaturation achieved in the instrument, which was 0.15%. Cloud supersaturations, which are taken as the supersaturation where half the residual particles activate, were not resolvable in these cases. Resolved spectra made up 34% of all the measurements taken when LWC was greater than 0.1 g $kg^{-1}$. From these resolved spectra, cloud supersaturations averaged $0.2 \pm 0.04\%$. This average should be considered as an upper bound on the mean supersaturation since it excludes supersaturations that were below the minimum measured by the instrument.

The SOLEDAD clouds were driven by the advection of marine clouds to the coast. All of the clouds were sampled during the night, as cooling of the ocean surface decreased the lifting condensation level below the Mount Soledad field site (251 m asl). During the three cloud events considered in this study (section 2.2.1), CDNC varied from below 10 up to 231 $cm^{-3}$ (Figure 5a). CCN concentrations at 0.1–0.15% supersaturation were generally higher and averaged $240 \pm 160$ $cm^{-3}$, which suggests cloud supersaturations were below 0.1–0.15%.

Like for the E-PEACE data set, SOLEDAD cloud supersaturations were also derived from CCN-CVI measurements. CCN concentrations were measured by two separate CCN counters operated in parallel behind the CVI inlet. One counter scanned over a supersaturation range from 0.1 to 0.74% every 10 min, while the other counter operated at a constant supersaturation of 0.3%. The ratio of 5 min averaged CCN concentrations at constant supersaturation of 0.3% to cloud droplet residual particle concentrations measured by a CPC was approximately 1 during all cloud events (Figure S7 in the supporting information), which indicates that supersaturations were less than 0.3%.

The CCN spectra were more difficult to interpret because there was significant variability in cloud droplet number concentration over the 10 min required to perform each scan. Nevertheless, the spectra measured when cloud droplet number concentrations were highest ($>25$ $cm^{-3}$) and least variable (standard

deviation/mean $< 0.8$) did not indicate clear activation thresholds, which suggests the ambient supersaturations were less than 0.1%, the lowest supersaturation achieved in the scanning CCN counter. Figure S7 in the supporting information shows that the ratio of 5 min averaged CCN concentrations over the supersaturation range 0.1–0.74% to cloud droplet residual particle concentrations was approximately 1 during all cloud events.

To further constrain the supersaturations of Clouds 2 and 3, *Schroder et al.* [2015] modeled the CCN activity of the cloud droplet residuals with kappa-Kohler theory [*Petters and Kreidenweis*, 2007]. As input, the calculations required measurements of the size distribution of cloud droplet residual particles (SMPS) and their chemical composition (HR-AMS). The average effective peak supersaturations for Clouds 2 and 3 derived using this method were 0.05%, which is consistent with the direct CCN-CVI measurements that suggested these values were less than 0.1%.

In summary, subtropical marine stratocumulus clouds were targeted in E-PEACE and SOLEDAD. Calculated supersaturations were lower in SOLEDAD ($<$0.1%) than E-PEACE ($0.2 \pm 0.04$%). It should be noted that the CCN-CVI supersaturation estimates assume no collision-coalescence of cloud droplets occurred or aqueous-phase cloud processing. Aqueous-phase processes would have added soluble material to the cloud residuals and decreased their critical supersaturations. Additionally, the CVI inlets only sampled larger cloud droplets ($D_p >$ ~11 μm). Therefore, supersaturations derived from the CCN-CVI measurements should be considered as lower limit estimates of the true ambient values. Nevertheless, given that observed cloud droplet number concentrations were comparable to or lower than CCN concentrations at low supersaturations (Figure 5a), these estimates seem reasonable. Consequently, we conclude that both the E-PEACE and SOLEDAD clouds belonged to the supersaturation regime in which PMA contributes substantially to cloud formation (supersaturation $<$ 0.3%).

#### 4.3.2. Comparison of E-PEACE and SOLEDAD PMA CCN Results

In E-PEACE, PMA CCN fractions as a function of supersaturation were measured at the ocean surface from the R/V *Point Sur* (Figure 5c). The CIRPAS Twin Otter measured average supersaturations of $0.2 \pm 0.04$% in the overlying stratocumulus. Combining the measured PMA concentrations and supersaturations, we estimate that during the high-PMA period (20–24 July), PMA contributed an average of 20–27% (range 5–58%) of the CCN seeding the stratocumulus clouds, with the range of averages dependent on the detailed chemical composition of the PMA-containing particles. However, during the low-PMA period from 12 to 20 July, the corresponding mean contributions were less than 10% (range 1–27%). To confirm that these estimates are reasonable, sea-salt concentrations in the cloud water samples collected on the Twin Otter averaged $8.1 \pm 6.8\ \mu g\ m^{-3}$ (±1 std. deviation) during the high-PMA period and $1.2 \pm 0.8\ \mu g\ m^{-3}$ during the low-PMA period. These values are higher than the submicrometer sea-salt concentrations reported in Figures 2 and 3 because the cloud water samples also contained contributions from supermicrometer sea-salt particles. Still the observed trend in cloud water sea salt is consistent with our estimated PMA CCN fractions.

For SOLEDAD, sea salt averaged on the order of 12–24% of the dried residual mass of the clouds. It is not meaningful to quantitatively compare the SOLEDAD mass fraction and E-PEACE number fraction measurements. Nevertheless, the combined results suggest that PMA can make major contributions to the CCN forming stratocumulus clouds in relatively clean marine regions, as well as in coastal areas subject to greater anthropogenic pollution influences. However, it must be recalled that in lower wind conditions encountered during E-PEACE, PMA typically formed less than 10% of total CCN, regardless of cloud supersaturations and the chemical composition of the PMA, and even when total aerosol concentrations were at clean marine levels (mean $664 \pm 45\ cm^{-3}$).

### 4.4. PMA Effects on CDNC

Due to competition for water vapor, an increase in the number of available CCN does not always lead to an increase in cloud droplet number concentrations (CDNC) [*Leaitch et al.*, 1986]. For example, coarse PMA particles uptake water so rapidly that they can reduce maximum supersaturations in clouds. Depending on the concentrations of other CCN mixed with the PMA, this process can lead to reduction of cloud droplet number concentration (CDNC) and enhancement of cloud droplet sizes and precipitation probabilities [*Ghan et al.*, 1998; *Rosenfeld et al.*, 2002; *Rudich et al.*, 2002; *Karydis et al.*, 2012]. This section investigates the effect of PMA on CDNC during E-PEACE and SOLEDAD.

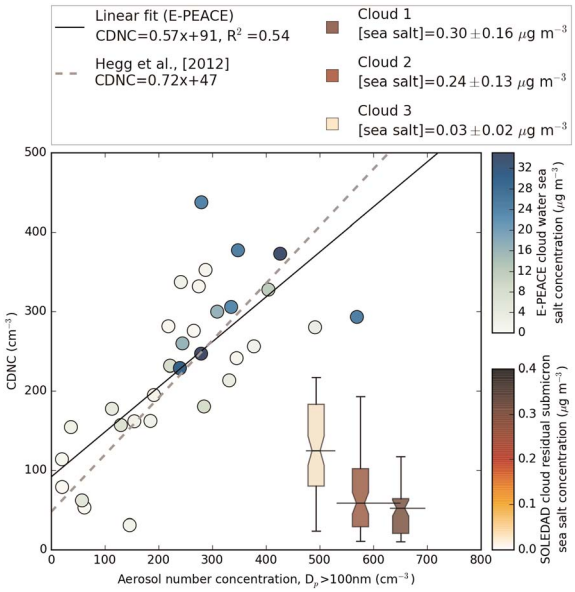


**Figure 7.** Cloud Droplet Number Concentration (CDNC) for droplets with diameters between 0.65 and 55 μm (E-PEACE) and 3 and 50 μm (SOLEDAD) versus number concentration of aerosol particles with diameter > 100 nm for E-PEACE and SOLEDAD. Markers are colored by sea-salt concentration in cloud water samples collected on the Twin Otter for E-PEACE, and sea-salt concentrations measured by HR-AMS in dried cloud droplet residuals sampled during SOLEDAD. The boxplot markers are centered at the average accumulation-mode aerosol concentration for each SOLEDAD cloud, with horizontal error bars representing the interquartile range of concentrations. The dashed grey line is the linear relationship between CDNC and accumulation-mode aerosol concentrations reported by *Hegg et al.* [2012], and the solid black line is a linear fit to the E-PEACE measurements. Full details of the data displayed in the plot can be found in section S6 in the supporting information. Further properties of the SOLEDAD clouds are summarized in Table 1.

*Hegg et al.* [2012] recently reported that the relationship between CDNC and subcloud accumulation-mode aerosol particle concentrations ($D_p > 100$ nm) is positive, linear, and remarkably constant for marine stratocumulus clouds off the Californian and Chilean coasts. The authors hypothesized the relationship is maintained by a buffer of available smaller and/or less hygroscopic particles that provides negative feedback to any perturbation in aerosol concentration. However, at sufficiently high aerosol concentrations, water vapor depletion will eventually lead to "roll-off" in the CDNC-aerosol relationship (i.e., further increases in subcloud aerosol concentrations result in less than proportional increases in CDNC). This has been observed in a number of studies [*Leaitch et al.*, 1992; *Glantz and Noone*, 2000; *Hegg et al.*, 2012]. The exact onset of roll-off will depend on cloud dynamics and the size and composition of CCN [*Leaitch et al.*, 1986; *Hegg et al.*, 2012].

This relationship provides a convenient framework for assessing the possibility that water vapor depletion by large-PMA particles had a negative effect on CDNC during E-PEACE and SOLEDAD. Figure 7 plots CDNC against accumulation-mode ($D_p > 100$ nm) particle concentrations for both campaigns, with markers colored by in-cloud sea-salt concentrations (submicrometer for SOLEDAD, while E-PEACE cloud water samples also contained contributions from supermicrometer particles). Full details of the plot are described in section S6 in the supporting information. E-PEACE CDNC values are averaged over the 10–30 min that was required to collect a cloud water sample, which means each data point represents a single cloud or a few adjacent clouds. In contrast, only three clouds from the entire SOLEDAD campaign were analyzed, but many HR-AMS sea-salt concentration measurements were taken in each cloud. Thus, the SOLEDAD data are represented in Figure 7 by boxplots with horizontal error bars to indicate the variability in CDNC and accumulation-mode particle concentration within each cloud. Other relevant SOLEDAD cloud properties are summarized in Table 1.

The E-PEACE measurements follow a positive linear relationship, similar to that reported by *Hegg et al.* [2012], independent of in-cloud sea-salt concentration. This suggests that the PMA particles had a net positive effect on CDNC during E-PEACE.

**Table 1.** Summary of Cloud Properties for the Three SOLEDAD Cloud Events: S Is Supersaturation Derived From CCN-CVI Measurements (Section 4.3.1); $N_{100}$ Is the Number Concentration of Aerosol Particles With Diameter > 100 nm (Figure 7 and Section S6 in the Supporting Information); CDNC Is the Concentration of Droplets With Diameters Between 3 and 50 μm; and LWC Is Liquid Water Content

| Cloud Event | S (%) | $N_{100}$ ($cm^{-3}$) | CDNC ($cm^{-3}$) | LWC ($g\,m^{-3}$) |
|---|---|---|---|---|
| 1 | <0.1 | 651 ± 53 | 47 ± 28 | 0.10 ± 0.05 |
| 2 | <0.1 | 576 ± 85 | 69 ± 47 | 0.13 ± 0.08 |
| 3 | <0.1 | 493 ± 46 | 125 ± 58 | 0.09 ± 0.03 |

The SOLEDAD results are more complex. First, CDNC were low relative to the concentrations of particles with $D_p > 100$ nm. All of the observations lie below the *Hegg et al*. [2012] relationship. This could indicates that the plot does not capture the true SOLEDAD precursor aerosol concentrations (in the absence of subcloud measurements, accumulation-mode aerosol concentration is represented by the in-cloud, total concentrations of interstitial particles plus cloud droplet residuals with $D_p > 100$ nm, section S6 in the supporting information), or that the very low supersaturation SOLEDAD clouds were in a different dynamical regime than the E-PEACE clouds.

It is more interesting that the three cloud-averaged SOLEDAD CDNC decreased with increasing precursor aerosol and in-cloud sea-salt concentrations. There was substantial variability within each of the three cloud events measured, but the differences in average CDNC and accumulation-mode aerosol concentration between the three clouds, and average sea-salt concentration in Cloud 3 compared to Clouds 1 and 2 were all statistically significant ($p < 0.05$, $n = 33$–$77$, Welch's $t$ test performed using the stats.ttest_ind function in the Python package SciPy). One possible explanation that is consistent with these observations is that coarse PMA particles reduced maximum supersaturations and prevented smaller particles from activating in Clouds 1 and 2, leading to the observed decrease in average CDNC with increasing precursor aerosol and in-cloud sea-salt concentrations. This effect may have been evident in the SOLEDAD clouds, but not the E-PEACE clouds, because supersaturations in the SOLEDAD clouds were lower and hence more sensitive to suppression by growth of large CCN [*Ghan et al*., 1998]. Consequently, the <0.1% supersaturations in each of the three clouds (Table 1 and section 4.3.1) may have been the result of both large-PMA and low-updraft velocities.

## 5. Conclusion

We have introduced a method for isolating PMA number size distributions from total aerosol size distributions and applied it to marine aerosol data collected on the R/V *Point Sur* off the coast of Monterey, California, during the E-PEACE field campaign. PMA number concentrations averaged $12 \pm 2\,\mathrm{cm}^{-3}$ during a relatively calm period from 12 to 20 July and $71 \pm 2\ \mathrm{cm}^{-3}$ during a higher wind speed period from 20 to 24 July. Collocated CCN measurements enabled calculation of the contribution of PMA to CCN as a function of supersaturation. PMA CCN fractions were highest at low supersaturations (<0.3%) and under the assumption that the PMA was completely inorganic (i.e., sea salt). With increasing supersaturation up to 0.9%, PMA CCN fractions decreased and also became less sensitive to the choice of PMA chemical composition (completely sea salt or organic). Supersaturations of $0.2 \pm 0.04\%$ were measured in the marine stratocumulus clouds that covered the E-PEACE study area. This means that, on average, PMA contributed 20–27% (range 5–58%) of the CCN that formed the clouds during the high-PMA period, and less than 10% (range 1–27%) to clouds during the low-PMA period.

Sea salt was measured directly in the residuals of dried cloud droplets sampled from Mount Soledad on the coast of California during SOLEDAD. The mass fractions of PMA in the residuals averaged on the order of 12 to 24%. This result indicates that PMA particles contributed to the CCN that formed the SOLEDAD clouds.

The net effect of a change in the number of available CCN on cloud droplet number concentrations depends on the CCN distribution and the dynamics of the cloud. Examination of the dependence of CDNC on precursor aerosol concentrations as a function of in-cloud sea-salt levels suggests that PMA had a positive impact on the cloud droplet number concentrations of the marine stratocumulus clouds probed during E-PEACE. However, PMA particles may have contributed to the reduction in CDNC with increasing >100 nm particles in the three clouds sampled during SOLEDAD, since supersaturation can be reduced by rapid water vapor depletion by coarse PMA particles.

**Acknowledgments**
This work was funded by NSF AGS-1360645, NSF AGS-1013423, NSF AGS-1008848, DOE DE-SC0006679, and ONR grants N00014-11-1-0783, N00014-10-1-0200, and N00014-10-1-0811. R.L.M. appreciates the support of the Scripps Postdoctoral Scholars program. We gratefully acknowledge the help and support of the crew and staff of the R/V *Point Sur* and the CIRPAS Twin Otter, as well as assistance from Janin Guzman-Morales, Ashley Corrigan, Bill Shull, and Ken Duff of Scripps Institution of Oceanography. To obtain the data used in this study please go to http://goo.gl/3lWlJz or contact the corresponding author (lmrussell@ucsd.edu).

## References

Andreae, M. O., and D. Rosenfeld (2008), Aerosol–cloud–precipitation interactions. Part 1. The nature and sources of cloud-active aerosols, *Earth Sci. Rev.*, *89*(1–2), 13–41, doi:10.1016/j.earscirev.2008.03.001.

Bates, T. S., D. J. Coffman, D. S. Covert, and P. K. Quinn (2002), Regional marine boundary layer aerosol size distributions in the Indian, Atlantic, and Pacific Oceans: A comparison of INDOEX measurements with ACE-1, ACE-2, and Aerosols99, *J. Geophys. Res.*, *107*(D19), 8026, doi:10.1029/2001JD001174.

Bates, T. S., et al. (2008), Boundary layer aerosol chemistry during TexAQS/GoMACCS 2006: Insights into aerosol sources and transformation processes, *J. Geophys. Res.*, *113*, D00F01, doi:10.1029/2008JD010023.

Bates, T. S., et al. (2012), Measurements of ocean derived aerosol off the coast of California, *J. Geophys. Res.*, *117*, D00V15, doi:10.1029/2012JD017588.

Blot, R., A. D. Clarke, S. Freitag, V. Kapustin, S. G. Howell, J. B. Jensen, L. M. Shank, C. S. McNaughton, and V. Brekhovskikh (2013), Ultrafine sea spray aerosol over the southeastern Pacific: Open-ocean contributions to marine boundary layer CCN, *Atmos. Chem. Phys.*, *13*(14), 7263–7278, doi:10.5194/acp-13-7263-2013.

Clarke, A. D., S. R. Owens, and J. Zhou (2006), An ultrafine sea-salt flux from breaking waves: Implications for cloud condensation nuclei in the remote marine atmosphere, *J. Geophys. Res.*, *111*, D06202, doi:10.1029/2005JD006565.

Clarke, A. D., S. Freitag, R. M. C. Simpson, J. G. Hudson, S. G. Howell, V. L. Brekhovskikh, T. Campos, V. N. Kapustin, and J. Zhou (2013), Free troposphere as a major source of CCN for the equatorial pacific boundary layer: Long-range transport and teleconnections, *Atmos. Chem. Phys.*, *13*(15), 7511–7529, doi:10.5194/acp-13-7511-2013.

Coggon, M. M., et al. (2012), Ship impacts on the marine atmosphere: Insights into the contribution of shipping emissions to the properties of marine aerosol and clouds, *Atmos. Chem. Phys.*, *12*(18), 8439–8458, doi:10.5194/acp-12-8439-2012.

Collins, D. B., et al. (2013), Impact of marine biogeochemistry on the chemical mixing state and cloud forming ability of nascent sea spray aerosol, *J. Geophys. Res. Atmos.*, *118*, 8553–8565, doi:10.1002/jgrd.50598.

Cravigan, L. T., Z. Ristovski, R. L. Modini, M. D. Keywood, and J. L. Gras (2015), Observation of sea-salt fraction in sub-100 nm diameter particles at Cape Grim, *J. Geophys. Res. Atmos.*, *120*, 1848–1864, doi:10.1002/2014JD022601.

De Bock, L. A., P. E. Joos, K. J. Noone, R. A. Pockalny, and R. E. V. Grieken (2000), Single particle analysis of aerosols, observed in the marine boundary layer during the Monterey Area Ship Tracks Experiment (MAST), with respect to cloud droplet formation, *J. Atmos. Chem.*, *37*(3), 299–329, doi:10.1023/A:1006416600722.

DeCarlo, P. F., et al. (2006), Field-deployable, high-resolution, time-of-flight aerosol mass spectrometer, *Anal. Chem.*, *78*(24), 8281–8289, doi:10.1021/ac061249n.

De Leeuw, G., E. L. Andreas, M. D. Anguelova, C. W. Fairall, E. R. Lewis, C. O'Dowd, M. Schulz, and S. E. Schwartz (2011), Production flux of sea spray aerosol, *Rev. Geophys.*, *49*, RG2001, doi:10.1029/2010RG000349.

Dinger, J. E., H. B. Howell, and T. A. Wojciechowski (1970), On the source and composition of cloud nuclei in a subsident air mass over the North Atlantic, *J. Atmos. Sci.*, *27*(5), 791–797, doi:10.1175/1520-0469(1970)027<0791:OTSACO>2.0.CO;2.

Finlayson-Pitts, B. J., and J. C. Hemminger (2000), Physical chemistry of airborne sea salt particles and their components, *J. Phys. Chem. A*, *104*(49), 11,463–11,477, doi:10.1021/jp002968n.

Fitzgerald, J. W. (1991), Marine aerosols: A review, *Atmos. Environ. Part A*, *25*(3–4), 533–545, doi:10.1016/0960-1686(91)90050-H.

Frossard, A. A., and L. M. Russell (2012), Removal of sea salt hydrate water from seawater-derived samples by dehydration, *Environ. Sci. Technol.*, *46*(24), 13,326–13,333, doi:10.1021/es3032083.

Frossard, A. A., L. M. Russell, S. M. Burrows, S. M. Elliott, T. S. Bates, and P. K. Quinn (2014), Sources and composition of submicron organic mass in marine aerosol particles, *J. Geophys. Res. Atmos.*, *119*, 12,977–13,003, doi:10.1002/2014JD021913.

Fuentes, E., H. Coe, D. Green, G. de Leeuw, and G. McFiggans (2010), On the impacts of phytoplankton-derived organic matter on the properties of the primary marine aerosol—Part 1: Source fluxes, *Atmos. Chem. Phys.*, *10*(19), 9295–9317, doi:10.5194/acp-10-9295-2010.

Ghan, S. J., G. Guzman, and H. Abdul-Razzak (1998), Competition between sea salt and sulfate particles as cloud condensation nuclei, *J. Atmos. Sci.*, *55*(22), 3340–3347, doi:10.1175/1520-0469(1998)055<3340:CBSSAS>2.0.CO;2.

Glantz, P., and K. J. Noone (2000), A physically-based algorithm for estimating the relationship between aerosol mass and cloud droplet number, *Tellus B*, *52*(5), 1216–1231, doi:10.1034/j.1600-0889.2000.01077.x.

Grythe, H., J. Ström, R. Krejci, P. Quinn, and A. Stohl (2014), A review of sea-spray aerosol source functions using a large global set of sea salt aerosol concentration measurements, *Atmos. Chem. Phys.*, *14*(3), 1277–1297, doi:10.5194/acp-14-1277-2014.

Hayden, K. L., A. M. Macdonald, W. Gong, D. Toom-Sauntry, K. G. Anlauf, A. Leithead, S.-M. Li, W. R. Leaitch, and K. Noone (2008), Cloud processing of nitrate, *J. Geophys. Res.*, *113*, D18201, doi:10.1029/2007JD009732.

Hegg, D. A., and P. V. Hobbs (1986), Sulfate and nitrate chemistry in cumuliform clouds, *Atmos. Environ.*, *20*(5), 901–909, doi:10.1016/0004-6981(86)90274-X.

Hegg, D. A., D. S. Covert, H. H. Jonsson, and R. K. Woods (2012), A simple relationship between cloud drop number concentration and precursor aerosol concentration for the regions of Earth's large marine stratocumulus decks, *Atmos. Chem. Phys.*, *12*(3), 1229–1238, doi:10.5194/acp-12-1229-2012.

Heintzenberg, J., D. C. Covert, and R. Van Dingenen (2000), Size distribution and chemical composition of marine aerosols: A compilation and review, *Tellus B*, *52*(4), 1104–1122, doi:10.1034/j.1600-0889.2000.00136.x.

Hobbs, P. V. (1971), Simultaneous airborne measurements of cloud condensation nuclei and sodium-containing particles over the ocean, *Q. J. R. Meteorol. Soc.*, *97*(413), 263–271, doi:10.1002/qj.49709741302.

Hoppel, W. A., G. M. Frick, and R. E. Larson (1986), Effect of nonprecipitating clouds on the aerosol size distribution in the marine boundary layer, *Geophys. Res. Lett.*, *13*(2), 125–128, doi:10.1029/GL013i002p00125.

Hudson, J. G., S. Noble, and V. Jha (2010), Stratus cloud supersaturations, *Geophys. Res. Lett.*, *37*, L21813, doi:10.1029/2010GL045197.

Iacobellis, S. F., and D. R. Cayan (2013), The variability of California summertime marine stratus: Impacts on surface air temperatures, *J. Geophys. Res. Atmos.*, *118*, 9105–9122, doi:10.1002/jgrd.50652.

Karydis, V. A., S. L. Capps, A. G. Russell, and A. Nenes (2012), Adjoint sensitivity of global cloud droplet number to aerosol and dynamical parameters, *Atmos. Chem. Phys.*, *12*(19), 9041–9055, doi:10.5194/acp-12-9041-2012.

Keene, W. C., et al. (2007), Chemical and physical characteristics of nascent aerosols produced by bursting bubbles at a model air-sea interface, *J. Geophys. Res.*, *112*, D21202, doi:10.1029/2007JD008464.

Khlystov, A., C. Stanier, and S. N. Pandis (2004), An algorithm for combining electrical mobility and aerodynamic size distributions data when measuring ambient aerosol special issue of aerosol science and technology on findings from the fine particulate matter supersites program, *Aerosol Sci. Technol.*, *38*(sup1), 229–238, doi:10.1080/02786820390229543.

Klein, S. A., and D. L. Hartmann (1993), The seasonal cycle of low stratiform clouds, *J. Clim.*, *6*(8), 1587–1606, doi:10.1175/1520-0442(1993)006<1587:TSCOLS>2.0.CO;2.

Koehler, K. A., S. M. Kreidenweis, P. J. DeMott, A. J. Prenni, C. M. Carrico, B. Ervens, and G. Feingold (2006), Water activity and activation diameters from hygroscopicity data—Part II: Application to organic species, *Atmos. Chem. Phys.*, *6*(3), 795–809, doi:10.5194/acp-6-795-2006.

Lawler, M. J., J. Whitehead, C. O'Dowd, C. Monahan, G. McFiggans, and J. N. Smith (2014), Composition of 15–85 nm particles in marine air, *Atmos. Chem. Phys.*, *14*(21), 11,557–11,569, doi:10.5194/acp-14-11557-2014.

Leaitch, W. R., J. W. Strapp, G. A. Isaac, and J. G. Hudson (1986), Cloud droplet nucleation and cloud scavenging of aerosol sulphate in polluted atmospheres, *Tellus B*, *38B*(5), 328–344, doi:10.1111/j.1600-0889.1986.tb00258.x.

Leaitch, W. R., G. A. Isaac, J. W. Strapp, C. M. Banic, and H. A. Wiebe (1992), The relationship between cloud droplet number concentrations and anthropogenic pollution: Observations and climatic implications, *J. Geophys. Res.*, *97*(D2), 2463–2474, doi:10.1029/91JD02739.

Leaitch, W. R., C. M. Banic, G. A. Isaac, M. D. Couture, P. S. K. Liu, I. Gultepe, S.-M. Li, L. Kleinman, P. H. Daum, and J. I. MacPherson (1996), Physical and chemical observations in marine stratus during the 1993 North Atlantic Regional Experiment: Factors controlling cloud droplet number concentrations, *J. Geophys. Res.*, *101*(D22), 29,123–29,135, doi:10.1029/96JD01228.

Lewis, E. R., and S. E. Schwartz (2004), *Sea Salt Aerosol Production: Mechanisms, Methods, Measurements, and Models—A Critical Review*, AGU, Washington, D. C.

Liu, S., D. A. Day, J. E. Shields, and L. M. Russell (2011), Ozone-driven daytime formation of secondary organic aerosol containing carboxylic acid groups and alkane groups, *Atmos. Chem. Phys.*, *11*(16), 8321–8341, doi:10.5194/acp-11-8321-2011.

Modini, R. L., B. Harris, and Z. D. Ristovski (2010), The organic fraction of bubble-generated, accumulation mode sea spray aerosol (SSA), *Atmos. Chem. Phys.*, *10*(6), 2867–2877, doi:10.5194/acp-10-2867-2010.

Modini, R. L., L. M. Russell, G. B. Deane, and M. D. Stokes (2013), Effect of soluble surfactant on bubble persistence and bubble-produced aerosol particles, *J. Geophys. Res. Atmos.*, *118*, 1388–1400, doi:10.1002/jgrd.50186.

Moore, R. H., and A. Nenes (2009), Scanning flow CCN analysis—A method for fast measurements of CCN spectra, *Aerosol Sci. Technol.*, *43*(12), 1192–1207, doi:10.1080/02786820903289780.

Murphy, D. M., J. R. Anderson, P. K. Quinn, L. M. McInnes, F. J. Brechtel, S. M. Kreidenweis, A. M. Middlebrook, M. Pósfai, D. S. Thomson, and P. R. Buseck (1998), Influence of sea-salt on aerosol radiative properties in the Southern Ocean marine boundary layer, *Nature*, *392*(6671), 62–65, doi:10.1038/32138.

Nenes, A., S. Ghan, H. Abdul-Razzak, P. Y. Chuang, and J. H. Seinfeld (2001), Kinetic limitations on cloud droplet formation and impact on cloud albedo, *Tellus B*, *53*(2), 133–149, doi:10.1034/j.1600-0889.2001.d01-12.x.

Noone, K. J., J. A. Ogren, J. Heintzenberg, R. J. Charlson, and D. S. Covert (1988), Design and calibration of a counterflow virtual impactor for sampling of atmospheric fog and cloud droplets, *Aerosol Sci. Technol.*, *8*(3), 235–244, doi:10.1080/02786828808959186.

Noone, K. J., et al. (2000a), A case study of ships forming and not forming tracks in moderately polluted clouds, *J. Atmos. Sci.*, *57*(16), 2729–2747, doi:10.1175/1520-0469(2000)057<2729:ACSOSF>2.0.CO;2.

Noone, K. J., et al. (2000b), A case study of ship track formation in a polluted marine boundary layer, *J. Atmos. Sci.*, *57*(16), 2748–2764, doi:10.1175/1520-0469(2000)057<2748:ACSOST>2.0.CO;2.

Osthoff, H. D., et al. (2008), High levels of nitryl chloride in the polluted subtropical marine boundary layer, *Nat. Geosci.*, *1*(5), 324–328, doi:10.1038/ngeo177.

Ovadnevaite, J., D. Ceburnis, M. Canagaratna, H. Berresheim, J. Bialek, G. Martucci, D. R. Worsnop, and C. O'Dowd (2012), On the effect of wind speed on submicron sea salt mass concentrations and source fluxes, *J. Geophys. Res.*, *117*, D16201, doi:10.1029/2011JD017379.

Petters, M. D., and S. M. Kreidenweis (2007), A single parameter representation of hygroscopic growth and cloud condensation nucleus activity, *Atmos. Chem. Phys.*, *7*(8), 1961–1971, doi:10.5194/acp-7-1961-2007.

Pierce, J. R., and P. J. Adams (2006), Global evaluation of CCN formation by direct emission of sea salt and growth of ultrafine sea salt, *J. Geophys. Res.*, *111*, D06203, doi:10.1029/2005JD006186.

Prabhakar, G., B. Ervens, Z. Wang, L. C. Maudlin, M. M. Coggon, H. H. Jonsson, J. H. Seinfeld, and A. Sorooshian (2014), Sources of nitrate in stratocumulus cloud water: Airborne measurements during the 2011 E-PEACE and 2013 NiCE studies, *Atmos. Environ.*, *97*, 166–173, doi:10.1016/j.atmosenv.2014.08.019.

Prather, K. A., et al. (2013), Bringing the ocean into the laboratory to probe the chemical complexity of sea spray aerosol, *Proc. Natl. Acad. Sci. U.S.A.*, *110*(19), 7550–7555, doi:10.1073/pnas.1300262110.

Quinn, P. K., and D. J. Coffman (1999), Comment on "Contribution of different aerosol species to the global aerosol extinction optical thickness: Estimates from model results" by Tegen et al, *J. Geophys. Res.*, *104*(D4), 4241–4248, doi:10.1029/1998JD200066.

Quinn, P. K., and T. S. Bates (2011), The case against climate regulation via oceanic phytoplankton sulphur emissions, *Nature*, *480*(7375), 51–56, doi:10.1038/nature10580.

Randles, C. A., L. M. Russell, and V. Ramaswamy (2004), Hygroscopic and optical properties of organic sea salt aerosol and consequences for climate forcing, *Geophys. Res. Lett.*, *31*, L16108, doi:10.1029/2004GL020628.

Roberts, G. C., and A. Nenes (2005), A continuous-flow streamwise thermal-gradient CCN chamber for atmospheric measurements, *Aerosol Sci. Technol.*, *39*(3), 206–221, doi:10.1080/027868290913988.

Roberts, G., G. Mauger, O. Hadley, and V. Ramanathan (2006), North American and Asian aerosols over the eastern Pacific Ocean and their role in regulating cloud condensation nuclei, *J. Geophys. Res.*, *111*, D13205, doi:10.1029/2005JD006661.

Rosenfeld, D., R. Lahav, A. Khain, and M. Pinsky (2002), The role of sea spray in cleansing air pollution over ocean via cloud processes, *Science*, *297*(5587), 1667–1670, doi:10.1126/science.1073869.

Rudich, Y., O. Khersonsky, and D. Rosenfeld (2002), Treating clouds with a grain of salt, *Geophys. Res. Lett.*, *29*(22), 2064, doi:10.1029/2002GL016055.

Russell, L. M., S. Takahama, S. Liu, L. N. Hawkins, D. S. Covert, P. K. Quinn, and T. S. Bates (2009), Oxygenated fraction and mass of organic aerosol from direct emission and atmospheric processing measured on the R/V *Ronald Brown* during TEXAQS/GoMACCS 2006, *J. Geophys. Res.*, *114*, D00F05, doi:10.1029/2008JD011275.

Russell, L. M., L. N. Hawkins, A. A. Frossard, P. K. Quinn, and T. S. Bates (2010), Carbohydrate-like composition of submicron atmospheric particles and their production from ocean bubble bursting, *Proc. Natl. Acad. Sci. U.S.A.*, *107*(15), doi:10.1073/pnas.0908905107.

Russell, L. M., et al. (2013), Eastern Pacific emitted aerosol cloud experiment, *Bull. Am. Meteorol. Soc.*, *94*(5), 709–729, doi:10.1175/BAMS-D-12-00015.1.

Salcedo, D., et al. (2006), Characterization of ambient aerosols in Mexico City during the MCMA-2003 campaign with Aerosol Mass Spectrometry: Results from the CENICA supersite, *Atmos. Chem. Phys.*, *6*(4), 925–946, doi:10.5194/acp-6-925-2006.

Schroder, J. C., S. J. Hanna, R. L. Modini, A. L. Corrigan, S. M. Kreidenwies, A. M. Macdonald, K. J. Noone, L. M. Russell, W. R. Leaitch, and A. K. Bertram (2015), Size-resolved observations of refractory black carbon particles in cloud droplets at a marine boundary layer site, *Atmos. Chem. Phys.*, *15*(3), 1367–1383, doi:10.5194/acp-15-1367-2015.

Seinfeld, J. H., and S. N. Pandis (2006), *Atmospheric Chemistry and Physics: From Air Pollution to Climate Change*, 2nd ed., John Wiley, Hoboken, N. J.

Sellegri, K., C. D. O'Dowd, Y. J. Yoon, S. G. Jennings, and G. de Leeuw (2006), Surfactants and submicron sea spray generation, *J. Geophys. Res.*, *111*, D22215, doi:10.1029/2005JD006658.

Shank, L. M., S. Howell, A. D. Clarke, S. Freitag, V. Brekhovskikh, V. Kapustin, C. McNaughton, T. Campos, and R. Wood (2012), Organic matter and non-refractory aerosol over the remote Southeast Pacific: Oceanic and combustion sources, *Atmos. Chem. Phys.*, *12*(1), 557–576, doi:10.5194/acp-12-557-2012.

Shingler, T., et al. (2012), Characterisation and airborne deployment of a new counterflow virtual impactor inlet, *Atmos Meas Tech*, *5*(6), 1259–1269, doi:10.5194/amt-5-1259-2012.

Sorooshian, A., Z. Wang, M. M. Coggon, H. H. Jonsson, and B. Ervens (2013), Observations of sharp oxalate reductions in stratocumulus clouds at variable altitudes: Organic acid and metal measurements during the 2011 E-PEACE campaign, *Environ. Sci. Technol.*, *47*(14), 7747–7756, doi:10.1021/es4012383.

Stokes, M. D., G. B. Deane, K. Prather, T. H. Bertram, M. J. Ruppel, O. S. Ryder, J. M. Brady, and D. Zhao (2013), A marine aerosol reference tank system as a breaking wave analogue for the production of foam and sea-spray aerosols, *Atmos Meas Tech*, *6*(4), 1085–1094, doi:10.5194/amt-6-1085-2013.

Swietlicki, E., et al. (2008), Hygroscopic properties of submicrometer atmospheric aerosol particles measured with H-TDMA instruments in various environments—A review, *Tellus B*, *60*, 432–469, doi:10.1111/j.1600-0889.2008.00350.x.

Takahama, S., A. Johnson, and L. M. Russell (2013), Quantification of carboxylic and carbonyl functional groups in organic aerosol infrared absorbance spectra, *Aerosol Sci. Technol.*, *47*(3), 310–325, doi:10.1080/02786826.2012.752065.

Toom-Sauntry, D., and L. A. Barrie (2002), Chemical composition of snowfall in the high Arctic: 1990–1994, *Atmos. Environ.*, *36*(15–16), 2683–2693, doi:10.1016/S1352-2310(02)00115-2.

Twohy, C. H., and J. R. Anderson (2008), Droplet nuclei in non-precipitating clouds: Composition and size matter, *Environ. Res. Lett.*, *3*(4), 045002, doi:10.1088/1748-9326/3/4/045002.

Wang, Z., A. Sorooshian, G. Prabhakar, M. M. Coggon, and H. H. Jonsson (2014), Impact of emissions from shipping, land, and the ocean on stratocumulus cloud water elemental composition during the 2011 E-PEACE field campaign, *Atmos. Environ.*, *89*, 570–580, doi:10.1016/j.atmosenv.2014.01.020.

Wonaschütz, A., et al. (2013), Hygroscopic properties of smoke-generated organic aerosol particles emitted in the marine atmosphere, *Atmos. Chem. Phys.*, *13*(19), 9819–9835, doi:10.5194/acp-13-9819-2013.

Woodcock, A. H. (1952), Atmospheric salt particles and raindrops, *J. Meteorol.*, *9*(3), 200–212, doi:10.1175/1520-0469(1952)009<0200:ASPAR>2.0.CO;2.

Zábori, J., M. Matisāns, R. Krejci, E. D. Nilsson, and J. Ström (2012), Artificial primary marine aerosol production: A laboratory study with varying water temperature, salinity, and succinic acid concentration, *Atmos. Chem. Phys.*, *12*(22), 10,709–10,724, doi:10.5194/acp-12-10709-2012.

Zhao, R., et al. (2014), Cloud partitioning of isocyanic acid (HNCO) and evidence of secondary source of HNCO in ambient air, *Geophys. Res. Lett.*, *41*, 6962–6969, doi:10.1002/2014GL061112.